Irrigation Science
https://doi.org/10.1007/s00271-024-00931-9

ORIGINAL PAPER

Evaluating the precise grapevine water stress detection using unmanned aerial vehicles and evapotranspiration-based metrics

V. Burchard-Levine[1] · I. Borra-Serrano[1] · J. M. Peña[1] · W. P. Kustas[2] · J. G. Guerra[1] · J. Dorado[1] · G. Mesías-Ruiz[1] · M. Herrezuelo[1] · B. Mary[1] · L. M. McKee[2] · A. I. de Castro[3] · S. Sanchez-Élez[4] · H. Nieto[1]

Received: 24 January 2024 / Accepted: 7 April 2024

Abstract

Precise irrigation management requires accurate knowledge of crop water demand to adequately optimize water use efficiency, especially relevant in arid and semi-arid regions. While unoccupied aerial vehicles (UAV) have shown great promise to improve the water management for crops such as vineyards, there still remains large uncertainties to accurately quantify vegetation water requirements, especially through physically-based methods. Notably, thermal remote sensing has been shown to be a promising tool to evaluate water stress at different scales, most commonly through the Crop Water Stress Index (CWSI). This work aimed to evaluate the potential of a UAV payload to estimate evapotranspiration (ET) and alternative ET-based crop water stress indices to better monitor and detect irrigation requirements in vineyards. As a case study, three irrigation treatments within a vineyard were implemented to impose weekly crop coefficient (Kc) of 0.2 (extreme deficit irrigation), 0.4 (typical deficit irrigation) and 0.8 (over-irrigated) of reference ET. Both the original Priestley-Taylor initialized two-source energy balance model (TSEB-PT) and the dual temperature TSEB (TSEB-2T), which takes advantage of high-resolution imagery to discriminate canopy and soil temperatures, were implemented to estimate ET. In a first step, both ET models were evaluated at the footprint level using an eddy covariance (EC) tower, with modelled fluxes comparing well against the EC measurements. Secondly, in-situ physiological measurements at vine level, such as stomatal conductance (g_{st}), leaf (Ψ_{leaf}) and stem (Ψ_{stem}) water potential, were collected simultaneously to UAV overpasses as plant proxies of water stress. Different variants of the CWSI and alternative metrics that take advantage of the partitioned ET from TSEB, such as Crop Transpiration Stress Index (CTSI) and the Crop Stomatal Stress Index (CSSI), were also evaluated to test their statistical relationship against these in-situ physiological indicators using the Spearman correlation coefficient (ρ). Both TSEB-PT and TSEB-2T CWSI related similarly to in-situ measurements (Ψ_{leaf}*: $\rho \sim 0.4$;* Ψ_{stem}*: $\rho \sim 0.55$).* On the other hand, stress indicators using canopy fluxes (i.e. CTSI and CSSI) were much more effective when using TSEB-2 T (Ψ_{leaf}*: $\rho = 0.45$;* Ψ_{stem}*: $\rho = 0.62$)* compared to TSEB-PT (Ψ_{leaf}*: $\rho = 0.18$;* Ψ_{stem}*: $\rho = 0.49$),* revealing important differences in the ET partitioning between model variants. These results demonstrate the utility of physically-based models to estimate ET and partitioned canopy fluxes, which can enhance the detection of vine water stress and quantitatively assess vine water demand to better manage irrigation practices.

✉ V. Burchard-Levine
vburchard@ica.csic.es

[1] Tech4Agro Group, Institute of Agricultural Sciences - CSIC, Madrid, Spain

[2] USDA-ARS, Hydrology and Remote Sensing Laboratory, Beltsville, MD, USA

[3] Environment and Agronomy Department, National Agricultural and Food Research and Technology Institute-INIA, Spanish National Research Council (CSIC), Madrid, Spain

[4] Instituto Madrileño de Investigación y Desarrollo Rural, Agrario y Alimentario (IMIDRA), Finca El Socorro, Ctra. Chinchón - Belmonte de Tajo, Colmenar de Oreja 28380, Madrid, Spain

Published online: 29 April 2024

Introduction

Water is often the main limiting resource for agricultural production in arid and semi-arid regions, with increasing climate variability and demand for crop products further exacerbating pressure on hydrological resources. Vineyards occupy a particular cultural and economic importance in the Mediterranean region (Limier et al. 2018) and its relevance has also increased globally in other semi-arid regions such as USA, South America, South Africa and Australia (OIV 2022). Irrigation practices are becoming increasingly widespread in vineyards, particularly to control deficit irrigation practices and, especially, in light of the increase of extreme heat and drought events due to climate change (Rienth and Scholasch 2019; Romero et al. 2022).

As such, the precise spatio-temporal detection of vine water status can provide valuable guidelines for agronomic management practices to optimize water use and grape production. This is notably relevant for regulated deficit irrigation practices, a common strategy in viticulture to control wine quality and production, which needs an accurate assessment of crop water needs at different phenological periods (Coombe and McCarthy 2000; Girona et al. 2006). Indeed, water availability is a major factor for regulating both quality and productivity in grapevines with photosynthesis being primarily affected by stomatal closure (Escalona et al. 2000). Remote sensing, especially based on thermal infrared (TIR) information, has shown great promise to monitor vine water stress in both space and time (Bellvert et al., 2014; Kustas et al. 2022). It is well established that the canopy temperature is a sensitive indicator of vegetation water status (Jackson et al. 1981), through the relationship between canopy temperature, stomatal conductance and transpiration. Indeed, transpiration, consuming part of the energy from incoming solar irradiance, results in the cooling of canopy leaves. Water stress causes stomatal closure, inducing a reduction of transpiration and an increase in canopy temperature. As such, canopy temperature based on TIR has been widely applied in remote sensing to monitor water stress, most commonly through the crop water stress index (CWSI) as proposed by Jackson et al. (1981). The CWSI is related to the difference between actual evapotranspiration (ET) and potential ET without water limitation (i.e. $CWSI = 1 - ET/ET_{pot}$) and is most commonly estimated empirically by applying threshold limits normalizing between canopy temperature conditions for a well-watered crop and that with maximum stress (Maes and Steppe 2012). However, this empirical approach is often limited to depict the spatial variability of a given area with the empirically derived thresholds being dependent of the structural characteristics of the vegetation, phenological stage and surrounding environmental conditions (Bellvert et al. 2015; Gonzalez-Dugo and Zarco-Tejada 2022; Maes and Steppe 2012).

Other remote sensing-based methods use TIR observations to estimate ET through physically-based approaches such as surface energy balance models. In recent studies, notably through the GRAPEX project (Kustas et al. 2018, 2019, 2022), great advances have been made in estimating ET in vineyards at different spatial scales using various adaptations of the Two-Source Energy Balance (TSEB, Norman et al. 1995) with input data ranging from tower-based proximal sensors (e.g. Kustas, et al. 2022) to spaceborne imagery (e.g. Knipper et al. 2019). TSEB is particularly useful to detect crop water status as it inherently partitions the energy balance between the vegetation canopy and soil, thus providing an estimate of vegetation transpiration. Indeed, Bellvert et al. (2020) demonstrated that TSEB-derived canopy transpiration had a more robust relationship with stem water potential compared to bulk (i.e., canopy + soil) fluxes, which may be influenced by the background soil/substrate conditions. In light of this, Nieto et al. (2022) proposed a set of alternative crop water stress indicators that took advantage of TSEB's ability to estimate canopy fluxes as well as describing a method to estimate leaf stomatal conductance (g_{st}) by inverting flux estimates from TSEB. Through this, the Crop Stomatal Stress Index (CSSI), relating actual g_{st} based on TSEB estimates and maximum g_{st}, was proposed using tower-based inputs and obtained stronger correlations with in-situ water stress proxies compared to the more traditional CWSI using bulk fluxes (Nieto et al. 2022).

While bulk flux estimates from TSEB are generally well modelled when compared to EC measurements, the modelled ET partitioning has shown less consistency with mixed results observed in the literature (Gao et al. 2023; Kool et al. 2021; Kustas et al. 2019). Indeed, Kool et al. (2021) showed that ET partitioning was sensitive to the estimation of soil heat flux, the simulated radiation partitioning between canopy and soil and the transpiration initialization method. The original TSEB algorithm (Norman et al. 1995) implemented a Priestley and Taylor (1972) framework for an initial transpiration estimate (TSEB-PT) but other TSEB refinements have implemented a Penman–Monteith (PM) initialization (Colaizzi et al. 2012, 2014) or dual-source Shuttleworth and Wallace (1985) (SW) initialization (Kustas, et al. 2022a, b). In certain cases, TSEB-PT was shown to effectively estimate canopy fluxes in vineyards (Kool et al. 2021; Nieto et al. 2022) but other studies reported larger uncertainties (Kustas et al. 2019). Kustas and Norman (1997) proposed the use of TIR measurements at multiple viewing angles to separate canopy and soil temperatures analytically, eliminating the need to parameterize the canopy transpiration through energy combination models. Indeed, using a similar approach but taking advantage of high-spatial resolution imagery, as those obtained from Unmanned Aerial Vehicles (UAVs), Nieto et al. (2019) proposed a

dual-temperature TSEB (TSEB-2T), which directly retrieves canopy and soil temperatures from the TIR imagery and, as such, does not need to parameterize an a priori transpiration estimate.

Indeed, there is a growing interest from the research community to further develop methods that take advantage of UAVs to detect water stress at fine spatial scales to implement precision agriculture practices (Bellvert et al. 2016; de Castro et al. 2021; Nassar et al. 2020; Nieto et al. 2019). The use of high spatial resolution imagery can isolate the flux signals at the plant level and allow to better understand the spatial variability of crop stress within plot scales. In addition, using physically-based models to derive ET at fine resolution allows to not only assess the spatio-temporal variability of water stress but also to quantitatively assess the vine water demand giving potentially better recommendations for irrigation inputs required for different production goals. As such, this study aimed to evaluate the capabilities of different crop water stress metrics derived from process-based surface energy balance models and high-resolution UAV imagery to detect within-plot water stress over an experimental vineyard. In this study, both the original TSEB-PT and TSEB-2 T were implemented and were, as a first step, evaluated against eddy-covariance (EC) tower measurements located at the study site, to assess the general accuracy and expected uncertainties of these models at the EC footprint level. Subsequently, different crop water stress metrics, taking advantage of both modelled bulk and canopy fluxes, were computed and examined against in-situ vine physiological measurements, such as stomatal conductance (g_{st}), leaf (Ψ_{leaf}) and stem (Ψ_{stem}) water potential, serving as in-situ vine water stress proxies at treatment/irrigation sector level. In fact, the discrimination of the transpiration signal from soil evaporation has potentially very high utility to viticulture since transpiration is linked to photosynthesis, and thus grape productivity, while soil evaporation may be seen as a loss of water from an agronomic point of view. This study allows us to better understand how these UAV and ET-based indicators relate to vine water stress and demand over a small area of interest, assessing its potential to support decision making processes with quantitative estimates of vine water demand to better implement the most appropriate irrigation regime depending on production objectives, such as applying deficit irrigation practices to control vine quality or to optimize water use efficiency and grape production.

Materials and methods

Study site

The study was implemented in a 0.5 ha vineyard (*Petit Verdot* variety) located at the 'El Socorro' experimental farm in central Spain (40.14 N 3.37 E, Belmonte de Tajo, Madrid, Spain; altitude 755 m.a.s.l.). The grapevines were planted following a 2 m inter-row spacing by 1.1 m inter-vine spacing, with rows oriented in the North–South direction. The area is characterized by a typical semi-arid continental Mediterranean climate with mean annual air temperatures of about 14 °C and average annual rainfall of 420 mm (Guerra et al. 2022). The soil is characterized as Calcic Haploxeralf (pH 8.4) with a clay-loam texture. The inter-rows were mowed with a flail mower (Guerra et al. 2022), leaving no cover crop understory. The grapevines were placed on a vertical shoot position (VSP) trellis system with the crop height reaching maximums of roughly 1.5 m. In 2021, a drip irrigation system was installed allowing to establish an experimental design of randomized blocks of three replications for three different irrigation treatments (Fig. 1). The three different irrigation treatments consisted on maintaining three different crop coefficient (Kc) compared to the reference ET (ET_0) as calculated by the FAO56 Penman–Monteith method (Allen et al. 1998) using daily meteorological data from the nearby *Chinchón* weather station of the Spanish Agroclimatic information systems for irrigation (SIAR, https://eportal.mapa.gob.es/websiar/SeleccionParametrosMap.aspx?dst=1). The typical deficit irrigation practice of the region maintains Kc values at around 0.4 throughout the growing season (Romero et al. 2016; Rallo et al. 2021). Therefore to induce a large contrast and variability of vine water stress in the experimental study, we implemented treatments that imposed an extreme deficit irrigation (0.2Kc; 20% of ET_0), typical deficit irrigation (0.4Kc; 40% of ET_0) and highly irrigated practices (0.8Kc; 80% of ET_0). Irrigation began during the grapevine flowering (early June) and ended prior to harvest (mid-September) and were adjusted weekly over the three treatments taking into account the weekly accumulated rainfall and reference ET. This study was implemented over two vine growing seasons in 2022 and 2023, with an average annual irrigation input of 93, 194 and 371 mm for the 0.2Kc, 0.4Kc and 0.8Kc treatments, respectively.

Data and instrumentation

For both 2022 and 2023, field campaigns were performed every 2 weeks between June and September. During each campaign, a UAV flight was performed during midday conditions (~ 11–13 UTC) with a thermal infrared (TIR) and multispectral visible-to-near-infrared (VNIR) sensors, in addition to a high-resolution visible (RGB) camera (see Sect. "UAV imagery"). An eddy-covariance (EC) tower was installed on August 4th 2022 to sample continuous flux and meteorological measurements at high temporal frequency (see Sect. "Flux and energy balance data"). In this study, we solely made use of UAV campaigns with simultaneous measurements from the EC tower to apply and evaluate the TSEB modelling methods, resulting in a total of eight UAV

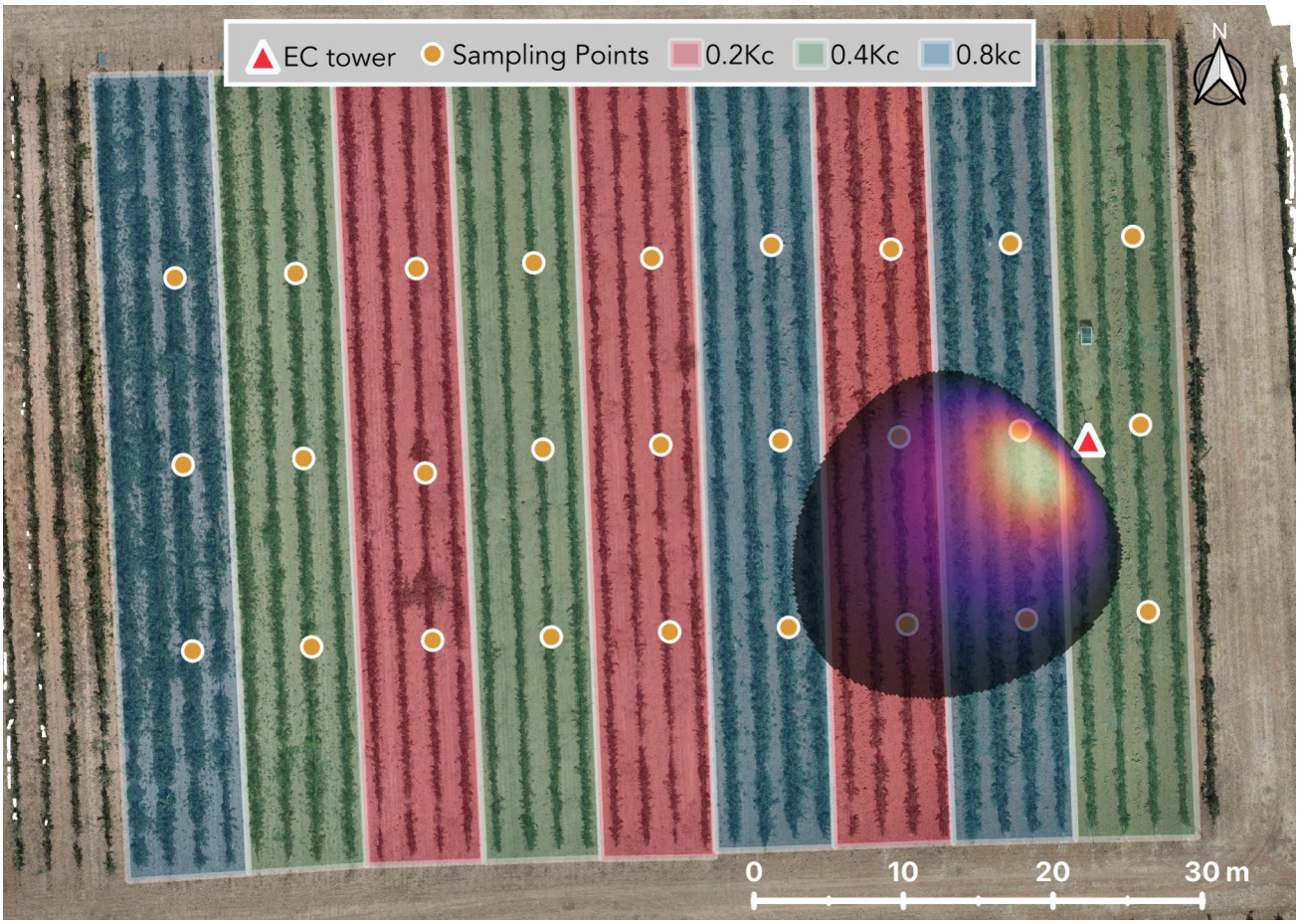

Fig. 1 Aerial view of the experimental scheme in 'El Socorro' farm with three different irrigation treatments and repetitions (0.2Kc in red, 0.4Kc in green and 0.8 Kc in blue) along with 27 permanent sampling points used to measure in-situ vine physiological measurements (orange circles) and location of eddy-covariance (EC) tower (red triangle) with the typical 2D footprint dimensions and weighted contribution to flux measurements where yellow-purple indicates a greater weight (estimated from Kljun et al. 2015 on 2022-08-30 11:00 UTC) directed towards the dominant southwest fetch. Orthomosaic taken from RGB camera camera (DJI P1) acquired on 2022-08-30

campaigns (Table 1). During each flight overpass, in-situ physiological data of leaf (Ψ_{leaf}) and stem (Ψ_{stem}) water potential, along with leaf stomatal conductance (g_{st}) were acquired to obtain a reference dataset of vine water stress during different phenological periods ranging from BBCH

Table 1 Date, UAV takeoff time, meteorological conditions during flight time and vine phenological stage according to BBCH scale (mode of in-situ observations) for each field campaign performed at El Socorro experimental farm. Meteorological data were acquired from EC tower installed within experimental farm

Date	UAV Takeoff time (UTC)	Air temperature (ºC)	Relative humidity (%)	Shortwave irradiance (W/m^2)	Wind speed (m/s)	Phenological stage (BBCH)	Three-day accumulated rainfall prior to campaign (mm)
2022-08-16	11:19	25.11	27	883	3.9	83	0
2022-08-30	11:23	28.80	31	843	3.4	85	0
2023-06-22	13:02	24.74	22	877	1.5	75	9.41
2023-07-04	13:03	30.69	40	981	3.6	77	0
2023-07-18	11:17	34.66	54	908	3.9	77	0
2023-08-01	11:38	31.03	44	959	2.4	79	0
2023-08-16	11:25	30.99	42	922	2.5	83	0
2023-08-29	11:39	23.24	25	856	3.6	85	0

scale (Lorenz et al. 1995) of 77 (fruit development) to 85 (Ripening of berries) (see Sect. "In-situ physiological data").

UAV imagery

A DJI Matrice-300 UAV (DJI Technology Co., Ltd, Shenzhen, China) was used to acquire VNIR, TIR and RGB imagery using the sensors Parrot Sequoia + (Parrot S.A., Paris, France), DJI's Zenmuse H20T and DJI's Zenmuse P1, respectively. The VNIR Sequoia + and TIR H20T acquired images simultaneous at 40 m above surface looking at nadir with 70 and 80% frontal and lateral overlap, resulting in a native pixel resolution of about 3–4 cm. The RGB images were acquired at 15 m above surface (also with 70 and 80% frontal and lateral overlap) to acquire a dense point cloud to do a 3D reconstruction through photogrammetric techniques.

UAV images were processed using OpenDroneMap (https://www.opendronemap.org/), an open-source drone processing software. Raw TIR H20T image tiles (i.e. in R-JPEG format) were first converted to single band radiometric temperatures using the open-source DJI Thermal SDK software (https://www.dji.com/downloads/softwares/dji-thermal-sdk). These individual temperature image tiles were then mosaicked together with OpenDroneMap. Congruently, multispectral images from Sequoia + were radiometrically calibrated using camera corrections, such as vignetting, black level and gain/exposure compensations, using the available routines developed for OpenDroneMap. (https://github.com/OpenDroneMap/ODM/blob/master/opendm/multispectral.py).

Flux and energy balance data

The EC and energy balance tower measurement system was located on the eastern edge of the experiment (Fig. 1) to have an adequate fetch from the dominant prevailing winds from the South-West. The tower was instrumented with an integrated open-path infrared gas analyzer and 3D Sonic anemometer Campbell Scientific[1] (IRGASON, Campbell Scientific, Logan, UT, USA) to measure ecosystem-level carbon and water gas exchanges. The raw data were sampled at a frequency of 20 Hz and recorded using a CR6 datalogger (Campbell Scientific, Logan, UT, USA). The Easyflux datalogger program (Easyflux-DL, Campbell Scientific, 2020) corrected the raw high-frequency data using the full suite of standard corrections and adjustments, including spike filtering, measurement quality control flags and applying correction for high/low frequency losses, to generate corrected half-hourly turbulent fluxes. More details of EC data post-processing are available in the EasyFlux-DL product manual (Campbell Scientific, 2020).

The full radiation budget, both shortwave and longwave, were measured using a four-component net radiometer (SN-500-SS, Apogee, Logan, UT, USA). Both EC and radiation instrumentation were installed on the tower at 3.3 m above ground level (agl) during the 2022 campaign and at 3.5 m agl during the 2023 campaign, over two times the maximum heights reached by the vine canopies. In addition, five soil heat flux plates (HFT-3, Radiation Energy Balance Systems, Bellevue, WA, USA) were installed along a cross-row southwest diagonal transect between the two vine rows following the dominant wind fetch (as shown in Fig. 1) each buried at 10 cm depth. This was done to characterize G conditions at different distances to the vine canopies but also takes into account the two outer rows of treatments 0.8Kc and 0.4Kc, which are the most dominant treatments within the flux footprint (Fig. 1). Five pairs of soil thermocouple probes (TCAV-L, Campbell Scientific, Logan, UT, USA) and five soil moisture sensors (CS655, Campbell Scientific, Logan, UT, USA) were co-located with each soil heat flux plate along the transect at depths of 2 and 8 and 5 cm depths, respectively for estimating storage term above the the heat flux plates.

Due to the well-known issue of the frequent lack of energy balance closure (EBC) from the EC system measurement technique, latent heat fluxes (LE) and sensible heat fluxes (H) were corrected, as described in Kustas et al. (2022), using the average of three typical closure methods: (1) assigning all residuals to LE, (2) assigning all residuals to H and (3) assigning residuals proportionally to LE and H maintaining the Bowen Ratio (i.e., H/LE). It is assumed that the ensemble mean comes closer to the 'true' observed flux values compared to any single correction method. This rationale is described and justified in Kustas et al. (2022) and Bambach et al. (2022). The energy balance closure (i.e. Rn-G vs H + LE) is shown in Fig. A1 for the entire sampling time of the EC measurements and for the specific time steps of the UAV overpasses, where the average closure ratio (H + LE/Rn-G) was 0.79 and 0.81, respectively.

In-situ physiological data

Midday leaf-level Ψ_{leaf}, Ψ_{stem} and g_{st} were acquired simultaneous to UAV overpass over 3 vines per treatment and block, resulting in a total of 27 evenly spaced sampling vines (3 treatments × 3 blocks × 3 vines) (Fig. 1). This resulted in a total of 72 and 54 measurements within each treatment for $\Psi_{leaf/stem}$ and g_{st}, respectively, with g_{st} only being sampled during the 2023 campaigns. Ψ_{leaf} and Ψ_{stem} were measured using a pressure chamber (Scholander et al. 1965), where

[1] The use of trade, firm, or corporation names in this article is for the information and convenience of the reader. Such use does not constitute official endorsement or approval by the US Department of Agriculture or the Agricultural Research Service of any product or service to the exclusion of others that may be suitable.

a well-developed sunlit leaf was excised in each sampled vine for the Ψ_{leaf} sample while the Ψ_{stem} sample was covered using an opaque aluminum bag prior to excision (at least one hour before sampling). Simultaneous to this, g_{st} was measured using the LI-600 porometer (LI-COR model 660, LI-COR Biosciences, Lincoln, NE, USA) by sampling six leaf samples per vine (three in the upper canopy and three in lower canopy). All three of these physiological measurements were acquired during midday conditions (between 11 and 13 UTC) simultaneous to UAV overpass.

TSEB-PT and TSEB-2 T models

Model descriptions

Remote sensing-based surface energy balance (SEB) models estimate LE as residual of the energy balance, relying on the ability of radiometric remote sensing information to estimate net radiation (Rn) and sensible heat flux (H), along with soil heat flux (G) usually as a proportion of Rn at the soil surface. There are different types of SEB models, broadly grouped between one-source models, which do not discriminate between soil and vegetation components over the surface, and multi-source models, which explicitly solves the energy balance over the different soil and vegetation sources. The main source of uncertainty in these models lies in the estimation of H, which is computed with the heat transport equation (Eq. 1).

$$H = \frac{\rho C_p \left(T_0 - T_A\right)}{R_{AH}} \tag{1}$$

where ρCp is the volumetric heat capacity of air (J m^{-3} K^{-1}), T_0 is the aerodynamic surface temperature (K), T_A is the air temperature at a reference height (K) and R_{AH} is the aerodynamic resistance to heat transport (s m^{-1}). This heat transport equation is only satisfied when using the conceptual aerodynamic surface temperature at the canopy source-sink height (i.e. T_0). However, the radiometric LST from remote sensing can differ significantly to $T_{0,}$ with their relationship not well establish and dependent on the surface and observation conditions (Colaizzi et al. 2004). One-source models therefore need to relate remotely sensed LST with T_0, often parameterizing additional resistance terms (Kustas et al. 2016) or applying empirical contextual methods (i.e., Allen et al. 2007) to account for these differences. By contrast, two-source models consider soil and vegetation sources separately within their framework, which explicitly accommodates the major factors that influence the relationship between radiometric LST and T_0, such as vegetation gap fraction and viewing angle. Indeed, the Two-Source Energy Balance (TSEB) model (Norman et al. 1995) is well established and has been shown to effectively simulate energy fluxes in vineyards, notably through the various scientific advances from the GRAPEX project (Kustas et al. 2018, 2019, 2022).

In TSEB, the energy balance is separated between a canopy (or vegetated) and soil sources (Eq. 2a, b), explicitly accounting for the aerodynamic coupling between the soil (subscript s) and vegetation canopy (subscript c) layers.

$$Rn, c = LEc + Hc \tag{2a}$$

$$Rn, s = LEs + Hs + G \tag{2b}$$

The radiative transfer through the canopy and soil (Rn,c and Rn, s) were estimated using an extinction coefficient approach as described in chapter 15 of Campbell and Norman (1998) and incorporated into TSEB by Kustas and Norman (1999). This is primarily dictated by the foliage density (i.e. LAI) and architecture of the vegetated canopy. In this case, we incorporated the clumping index taking into account the row structure of the grapevines, simulating them as simplified clumped rectangular canopies as described in Nieto et al. (2019). On the other hand, the ratio approach was used to model G, where it was estimated as 20% of the net radiation reaching the soil (Rn,s).

To decompose the energy balance, TSEB must separate the radiometric land surface temperature (LST) into its vegetation and soil components, assuming that the total temperature emitted by the surface is the combined emission of both vegetation and soil sources weighted by the fraction of vegetation canopy observed by the sensor (Eq. 3).

$$LST(\theta) = \left[f(\theta, LAI)T_c^4 + (1 - f(\theta, LAI))T_s^4\right]^1/4 \tag{3}$$

where $f(\theta)$ is the fraction of vegetation observed by the TIR sensor looking at a zenith angle θ, which also depends on LAI (Kustas and Norman 1999); T_c is the vegetation canopy temperature (K) and T_s is the soil substrate temperature (K).

Since both T_c and T_s are unknown a priori in Eq. 3, different approaches have been developed to estimate both component temperatures to solve the series of equations in TSEB. In this study, we make use of two approaches: the original modeling scheme based on a Priestley-Taylor (PT) initialization (TSEB-PT, Norman et al. 1995) and the contextual retrieval of both component temperatures using high resolution imagery Nieto et al. 2019).

TSEB-PT initializes the model by assuming, as a first guess, that the photosynthetically active part of the vegetation is transpiring at a potential rate (Eq. 4) and iteratively accounts for vegetation water stress until conservation of energy and temperature is achieved assuming daytime constraints and LST as a boundary condition.

$$LEc = \alpha_{PT} f_g \frac{\Delta}{\Delta + \gamma} Rn, c \tag{4}$$

where α_{PT} is the Priestley–Taylor coefficient, initially set to 1.26 but automatically reduced in TSEB-PT until convergence is reached, f_g is the fraction of vegetation that is photosynthetically active, Δ is the slope of the saturation vapour pressure versus temperature and γ is the psychrometric constant. For more details regarding the TSEB-PT model scheme, the reader is referred to Norman et al. (1995) and Kustas and Norman (1999).

For the TSEB-2 T implementation, T_c and T_s were directly retrieved using high resolution UAV imagery (see Sect. "TSEB implementation with UAV imagery"). This removes the need for a parametrization of the initial canopy transpiration of Eq. 4 and was originally proposed by Kustas and Norman (1997) using multiple TIR viewing angles. For more details regarding TSEB-2 T using UAV imagery, the reader is referred to Nieto et al. (2019a).

TSEB implementation with UAV imagery

The TSEB model runs were implemented by resampling the original UAV orthomosaics to 2 m pixel size, which is roughly the width of the grapevine rows. We assume that this spatial resolution is compatible with aerodynamic and radiation formulations applied within TSEB to be consistent with micro-meteorological lengths scales (Xia et al. 2016) and, therefore, contain both the vine canopy and soil inter-row at the pixel level.

Ancillary canopy structural variables are required in TSEB to account for both radiation transmission in row crops and turbulent heat exchange between the soil, plant and the atmosphere (Parry et al. 2019, Raupach 1994). Canopy height (CH) was estimated by generating the digital terrain model (DTM) and the digital elevation model (DEM) using photogrammetric techniques from the overlapping UAV-based RGB images (i.e. CH = DEM – DTM). CH was then resampled by extracting the maximum value within the 2 × 2 m pixel window.

Vegetation fractional cover (*fc*) was estimated from the classification of vine pixels at 0.03 m using a supervised classification (random forest classification) and further limited to pixels with normalized-difference-vegetation-index (NDVI) greater than 0.3 (limiting edge effects) and CH greater than 0.5 m to avoid non-vine vegetation (i.e. weeds) present in the interrows. Then, f_c was obtained from the fraction of vine pixels identified across the 2 × 2 m window. Similarly, T_c and T_s, needed for TSEB-2 T, were estimated by acquiring the mean of pixels classified as vine and soil, respectively within the 2 × 2 m window.

Finally, the leaf area index (LAI) at 2 m pixel resolution was estimated by developing a random forest regression model based on in-situ LAI measurements acquired at the sampling points shown in Fig. 1 using VNIR vegetation indices (OSAVI, Rondeaux et al. 1996 and reNDVI, Gitelson and Merzlyak 1994) and structural metrics (CH, *fc*) as predictor variables. Refer Fig. A1 to see the calibration and validation of the LAI model. During each campaign, *in-situ* LAI measurements were acquired over the 27 vine sampling points (Fig. 1) using the LAI-2200C (LI-COR, Biosciences, Lincoln, NE, USA) following the protocol developed by White et al. (2019) for vineyards. In this case, four measurements were performed at each of the 27 sampling point below the vine-row and then 1⁄4, 1⁄2 and 3⁄4 distance from vine-row to obtain an 'ecosystem'-level (i.e. vine + interrow) LAI reference. These references values were used to train the empirical model as similarly implemented by Kang et al. (2022) (see Fig. A2 for the LAI model training and testing).

Crop water stress metrics

From the TSEB outputs, different crop water stress indices were estimated and applied in this study to evaluate which indices were more related to in-situ physiological measurements. Traditionally, the Crop Water Stress Index (CWSI), based on the relationship between actual and potential evapotranspiration (Jackson et al. 1981), has been widely used to detect water stress from thermal remote sensing imagery. However, as discussed in Nieto et al. (2022) other stress indicators can also be generated taking advantage that two-source models, such as TSEB, separating canopy and soil fluxes. Nieto et al. (2022) proposed the Crop Transpiration Stress Index (CTSI, Eq. 5a) and Crop Stomatal Stress Index (CSSI, Eq. 5b).

$$CTSI = \frac{LEc}{LEc,sw} \tag{5a}$$

$$CSSI = \frac{g_s}{g_{st,0}} \tag{5b}$$

where LEc,sw is the potential canopy latent heat flux computed by Shuttleworth-Wallace model (Shuttleworth and Wallace 1985) (described in appendix B) and $g_{st,0}$ is the maximum stomatal conductance (see Nieto et al. 2022 for its derivation). Effective g_{st} can be estimated from TSEB modelled fluxes and aerodynamic resistances as demonstrated by Nieto et al. (2022). This is done by deriving the effective resistance to water vapour diffusion exerted by all leaves (R_c, Eq. 6)

$$R_c = \frac{\rho_a C_p \left(e_L - e_0\right)}{LEc\gamma} - R_x \tag{6}$$

where ρ_a is the air density, e_L is water vapour pressure in the leaf, which is assumed saturated at leaf temperature T_c (Farquhar and Sharkey 1982), e_0 is the vapour pressure of the air

at the canopy interface, related to air vapour pressure (e_a) measured at reference height as $e_0 = e_a + \frac{LE\gamma R_a}{p_a C_p}$ and R_x is the resistance to momentum and heat transport at the boundary layer of the canopy interface (see Norman et al. 1995 for details). As such, effective leaf-level g_{st} is estimated by inverting Eq. 7 (Kustas et al. 2022)

$$R_c = \frac{1}{f_t f_g LAI g_{st}} \tag{7}$$

where f_t is either 1 or 2 depending on stomatal distribution in the leaves (1 for hypostomatous and 2 for amphistomatous leaves).

Along with these stress indices that take advantage of partitioned LE, more traditional indices were also computed such as the Crop Water Stress Index using the one-source or big-leaf Penman–Monteith formulation to estimate potential LE (Eq. 8a, CSWI-PM), using the two-source Shuttleworth-Wallace formulation to estimate potential LE (Eq. 8b, CWSI-SW) and the widely used evaporative stress index (Eq. 8c, ESI; Anderson et al. 2007), which uses the FAO56 reference ET (Allen et al. 1998) to normalize the actual ET. The Penman–Monteith and Shuttleworth-Wallace energy combination equations are described in Appendix B.

$$CWSI\text{-}PM = \frac{\mathrm{LE}}{LE_{PM}} \tag{8a}$$

$$CWSI\text{-}SW = \frac{\mathrm{LE}}{LE_{SW}} \tag{8b}$$

$$ESI = \frac{\mathrm{LE}}{LE_{fao56}} \tag{8c}$$

Both LE_{PM} and LE_{SW} use a minimum stomatal resistance dependant on the vapour pressure deficit (VPD) as derived and detailed in Nieto et al. (2022) and Kustas et al. (2022).

Model evaluation

Modelled fluxes from both TSEB-PT and TSEB-2T were evaluated against tower measurements using the eddy-covariance (EC) technique. The two-dimensional EC footprint areas were estimated following the method described in Kljun et al. (2015) during the time step of the image acquisition, including estimating the footprint probability density function. Winds were often light and conditions were strongly unstable resulting in a relatively small footprint (Fig. 1) given the EC measurement height to canopy height ratio of ~ 2. The mean of the instantaneous modelled fluxes (LE, H, Rn and G) of all pixels located within the footprint were weighted by the normalized probability density function and evaluated against EC tower measurements.

In addition, modelled g_{st} based on TSEB-based LEc inversion were compared against in-situ g_{st} measured with the LI-600 porometer over sampled vines (Sect. "In-situ physiological data", Fig. 1). Model performance was evaluated based on the root-mean-square-error (RMSE, Eq. 9a), the relative RMSE (rRMSE, Eq. 9b), the mean bias (bias, Eq. 9c) and Pearson correlation coefficient (r, 9d).

$$RMSE = \sqrt{\frac{\sum \left(Y_{obs} - Y_{mod}\right)^2}{N}} \tag{9a}$$

$$rRMSE = \frac{RMSE}{Y_{obs,max} - Y_{obs,min}} \tag{9b}$$

$$bias = \frac{\sum \left(Y_{mod} - Y_{obs}\right)}{N} \tag{9c}$$

$$r = \frac{\sum \left(\left(Y_{mod} - Y_{mod,mean}\right)\left(Y_{obs} - Y_{obs,mean}\right)\right)}{\sqrt{\sum \left(\left(Y_{mod} - Y_{mod,mean}\right)^2\right) \sum \left(\left(Y_{ivs} - Y_{obs,mean}\right)^2\right)}} \tag{9d}$$

$$\rho = 1 - \frac{6 \sum d_i^2}{N(N^2 - 1)} \tag{9e}$$

where Y_{obs} are the observed values, Y_{mod} are the modelled values, N is the sample size and d_i represents the difference between the ranks of corresponding variables in the two datasets.

To understand how sensitive the modelled fluxes were to the irrigation treatments over the study area, a one-way analysis of variance (ANOVA) was performed to test whether the distribution of values between irrigation regimes were statistically different. In this case, we report both the F value, the ratio of variances where a high value indicates that the variance between treatment means was larger than the variance within treatment groups, and the p value, which quantifies the probability of obtaining such a F value if null hypothesis were true (i.e. that the distribution of values from the different treatments are the same). In addition, the different TSEB-based stress metrics were compared to in-situ physiological measurements and their relation was quantified through the Spearman rank correlation coefficient (ρ, Eq. 9e), which is a non-parametric measure of the monotonic relationship of variables, to account for possible non-linear relationships.

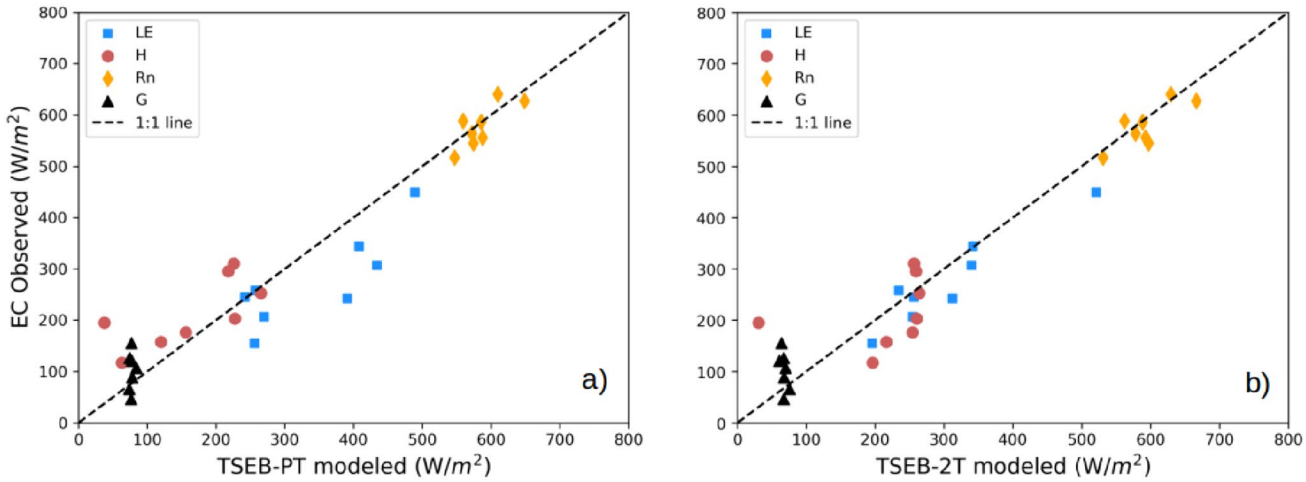

Fig. 2 Evaluation of modelled fluxes from TSEB-PT (**a**) and TSEB-2 T (**b**) against eddy-covariance (EC) observations

Table 2 Model performance indicators of root-mean-square-error (RMSE), relative RMSE (rRMSE), bias and pearson's correlation coefficient (r) for TSEB-PT and TSEB-2T against tower measurements

	TSEB-PT				TSEB-2 T			
	RMSE (W m^{-2})	rRMSE (%)	bias (W m^{-2})	r (–)	RMSE (W m^{-2})	rRMSE (%)	bias (W m^{-2})	r (–)
Rn	25	20	7	0.79	29	23	15	0.79
H	74	38	−49	0.72	79	41	3	0.34
LE	85	29	67	0.83	44	15	31	0.94
G	50	31	−10	−0.34	56	35	−20	−0.76

Results

Evaluation of TSEB-PT and TSEB-2T

In Fig. 2, the instantaneous flux estimates from both TSEB-PT (Fig. 2a) and TSEB-2 T (Fig. 2b) were plotted against EC measurements over the study area. In general, both TSEB variants performed similarly, with error metrics within comparable ranges (Table 2), although LE (H) was more systematically overestimated (underestimated) with TSEB-PT compared to TSEB-2 T. H was generally well modelled by TSEB-2T (RMSE = 79 Wm^{-2}; bias = 3 Wm^{-2}), but was more consistently underestimated by TSEB-PT (bias = −49 Wm^{-2}). By consequence, TSEB-PT modelled LE was more overestimated (RMSE = 85 Wm^{-2}; bias = 67 Wm^{-2}) compared to TSEB-2T (RMSE = 44 Wm^{-2}; bias = 31 Wm^{-2}), as well as being less correlated (r = 0.83 vs 0.94). In general, both models simulated Rn and G with low systematic errors. However, Rn was somewhat more overestimated by TSEB-2T (bias = 15 Wm^{-2}) while having a greater negative G bias (−20 Wm^{-2}), resulting in an overall larger overestimation of available energy (AE, Rn—G). This led to a modest systematic LE bias (31 Wm^{-2}) for TSEB-2 T even though H was largely in line with EC measurements (bias = 3 Wm^{-2}). For TSEB-PT, the AE was less overestimated but the larger H bias (−33 Wm^{-2}) led to a more consistent LE overestimation (bias = 47 Wm^{-2}). It should be noted that only eight UAV flights were used, therefore overall error metrics were sensitive to any significant discrepancies from one day. For example, TSEB-2 T H estimates from 2023-06-22 showed a larger bias compared to the other dates, increasing the scatter of errors. Indeed, while the average energy balance closure (i.e. [LE + H]/[Rn – G]) during the UAV overpass time steps was 0.81, the energy balance closure on 2023-06-22 was one of the lowest at 0.58. This may be a factor in the observed biases as the correction method has a more important weight leading to greater possible uncertainties in the observations than the model estimates. It also should be mentioned that the EC measurements are influenced by sources from both the 0.8Kc and 0.2Kc treatments, thus the model validation should be considered more qualitatively as an indicator that the models provide satisfactory flux estimates.

LE spatial distribution and irrigation treatment effects

In general, different LE distributions were detected over the study area as a consequence of the different irrigation regimes (Fig. 3). Modelled LE showed a distinct spatial

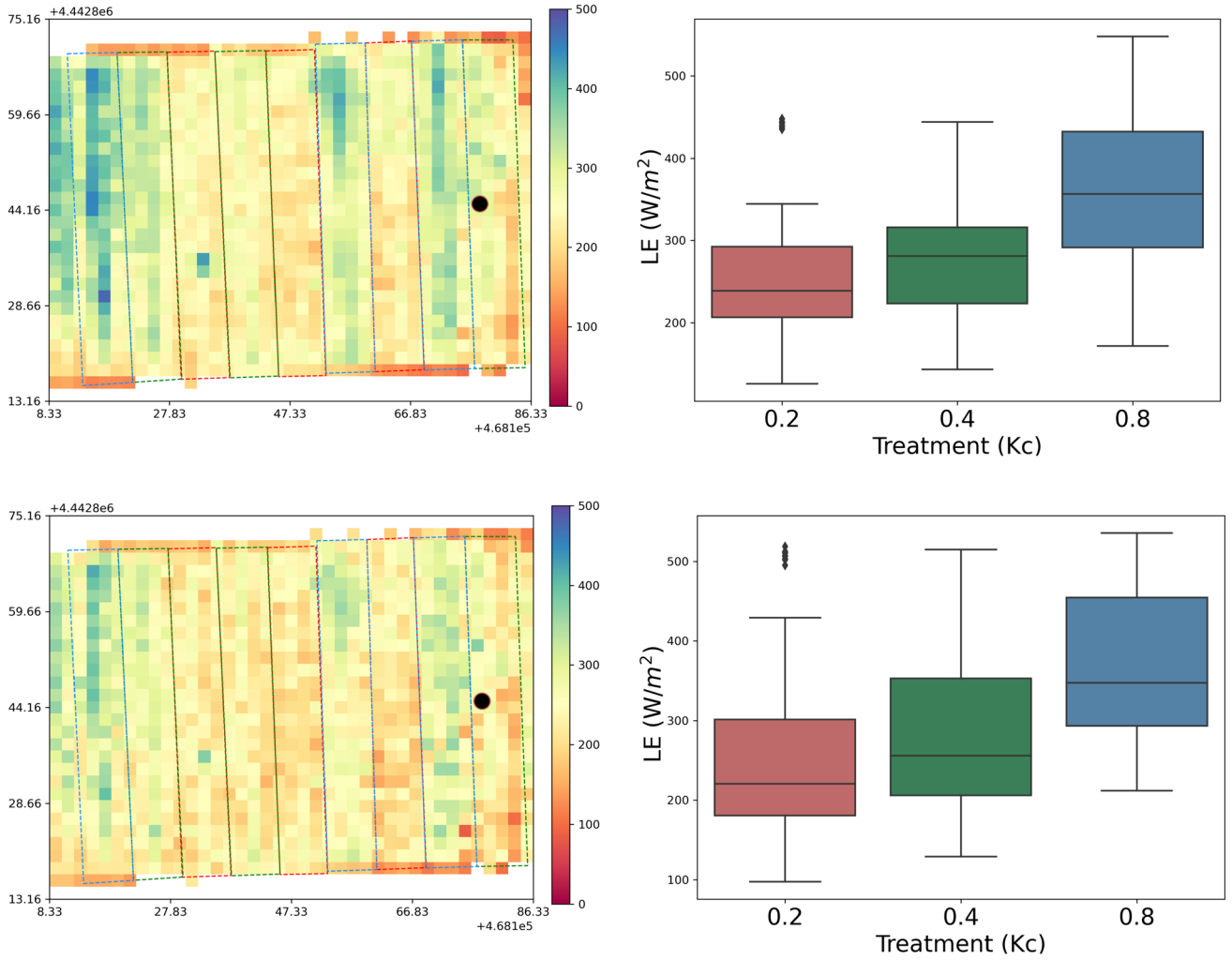

Fig. 3 TSEB-PT (top row) and TSEB-2T (bottom row) modelled latent heat flux (LE) on 2023-08-16 11:30 UTC over study area (left column) and corresponding boxplots for all dates grouped by 0.2 (red), 0.4 (green) and 0.8 (blue) Kc treatments (right column). The eddy-covariance (EC) tower is depicted by a black circle. The coordinates on X–Y axis are projected in UTM zone 30N with units in meters

distribution due to different irrigation regimes, with visually distinct spatial patterns observed in the map in Fig. 3 for both TSEB-PT and TSEB-2 T. This is supported quantitatively by the boxplots in Fig. 3 showing different distribution of values for each irrigation regime, where an ANOVA test revealed significant treatment effects for LE for both TSEB-PT (F value = 35.83; *p* value = 1.65e-14) and TSEB-2T (F value = 24.71; *p* value = 1.59e-10). Pairwise z-tests between each pair of treatments also revealed significantly different LE distributions for all pairs (*p* value < 0.001), except between 0.2 and 0.4 Kc treatment for TSEB-2T (*p* value = 0.16). By contrast, TSEB-PT modelled LE were significantly different between 0.2 and 0.4 Kc treatments (*p* value = 0.04), as well as all other treatment pairs (*p* value < 0.001).

While LE estimates from TSEB-PT and TSEB-2T were relatively similar, much greater contrast was observed for the modelled LE partitioning (LEc/LE). As Fig. 4 shows, TSEB-PT's median LEc/LE oscillated around 0.4 for all treatments, much lower than TSEB-2T's LEc/LE, which treatment median ranged roughly between 0.7 and 0.9. This was due to the important differences in estimated canopy and soil temperatures between both TSEB variants (Fig. 5). In general, the canopy (soil) temperature used in TSEB-2T were roughly 4 degrees cooler (hotter) than those estimated from TSEB-PT (Fig. 5). By using LEc/LE estimates, TSEB-2T outputs were found to have more significant treatment effects (F value = 18.71; *p value* = 2.77e-08) compared to TSEB-PT (F value = 7.21; *p value* = 0.0009). TSEB-2T had significant differences for all pairwise comparisons (*p value* < 0.05) while TSEB-PT had generally higher *p values*

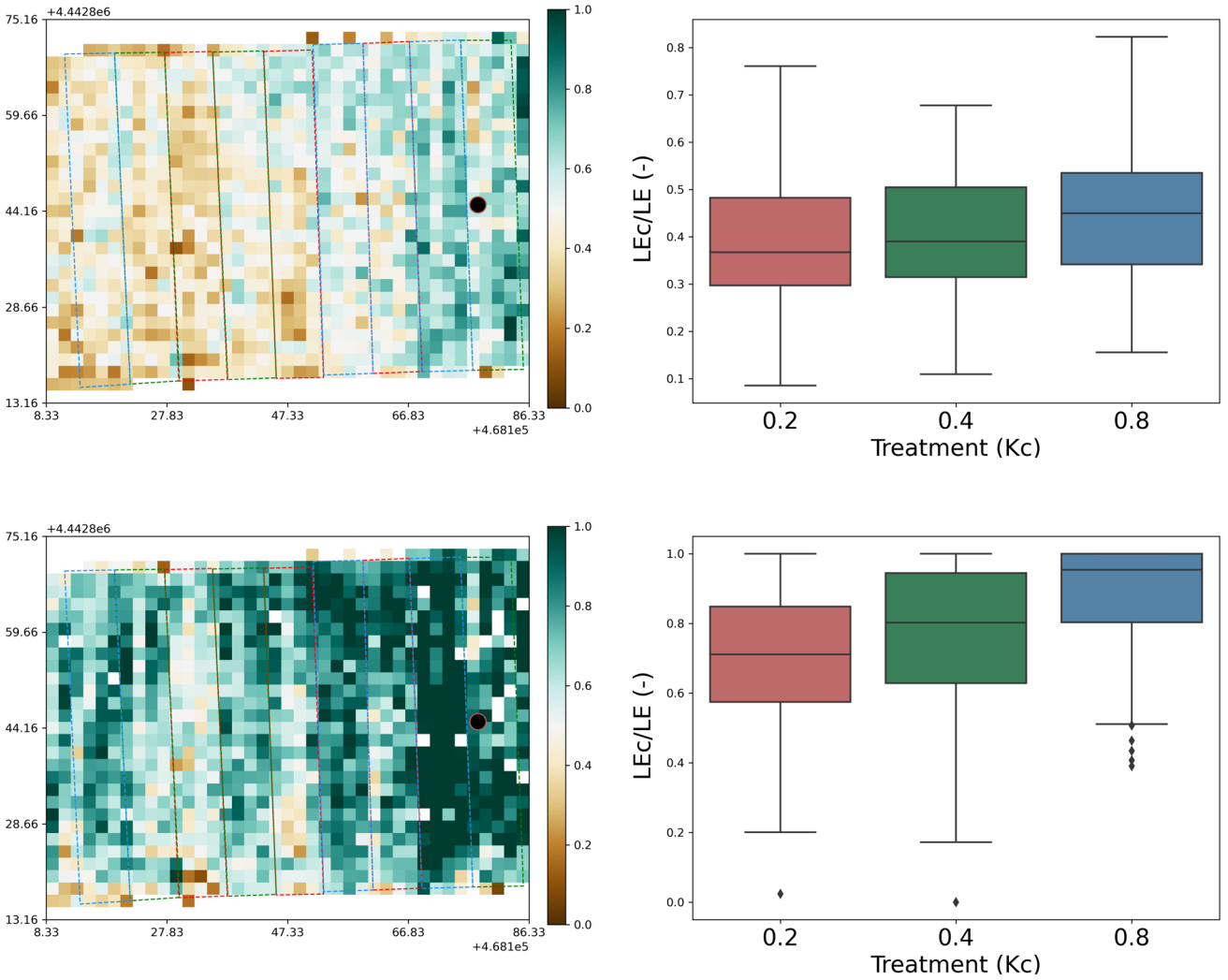

Fig. 4 TSEB-PT (top row) and TSEB-2T (bottom row) modelled latent heat flux (LE) partitioning (LEc/LE) on 2023-08-16 11:30 UTC over study area (left column) and corresponding boxplots for all dates grouped by 0.2 (red), 0.4 (green) and 0.8 (blue) Kc treatments (right column). Eddy-covariance (EC) tower is depicted by a black circle. The coordinates on X–Y axis are projected in UTM zone 30N with units in meters

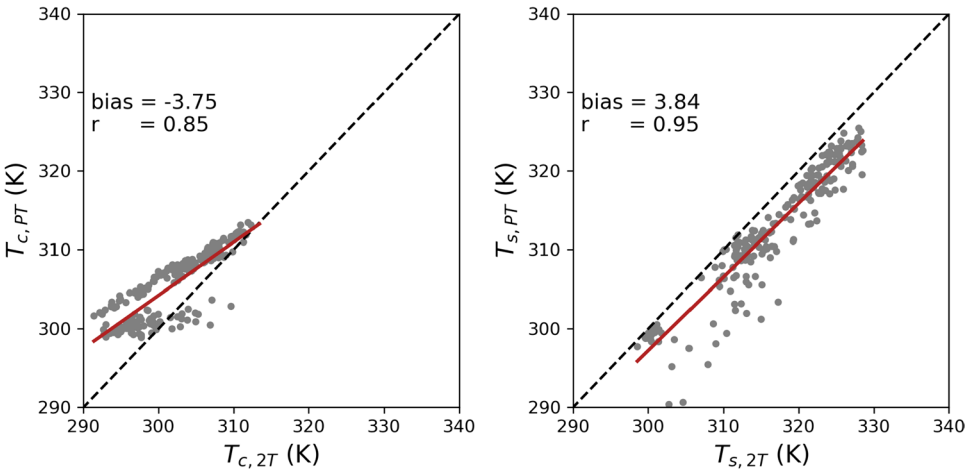

Fig. 5 Comparison between the estimated canopy (Tc, left panel) and soil (Ts, right panel) temperatures estimated by TSEB-PT and those applied in TSEB-2T over the 27 sampling points for all campaigns assessed

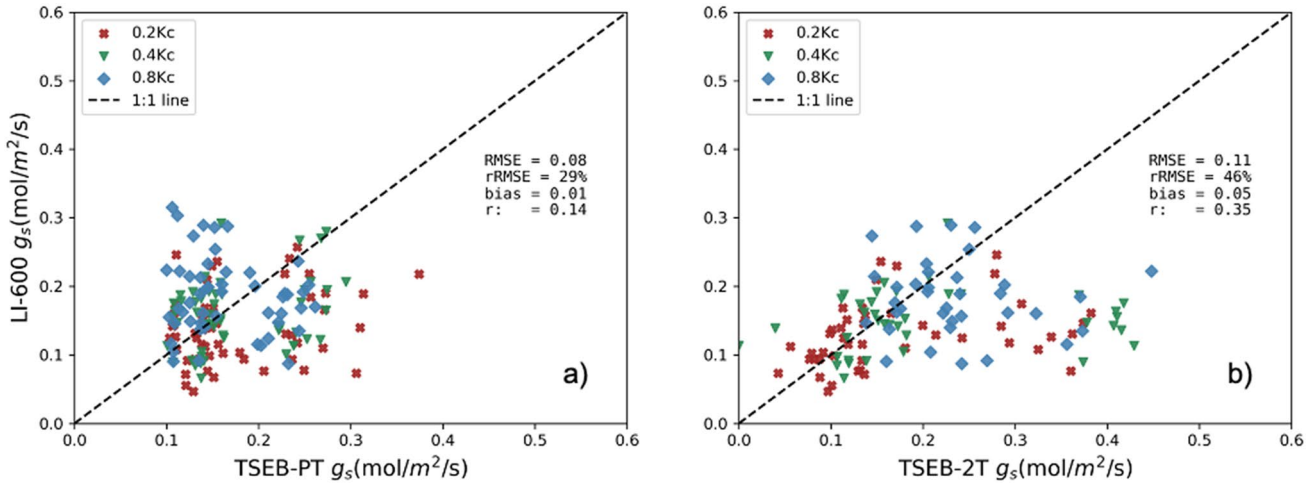

Fig. 6 Evaluation of TSEB-PT (**a**) and TSEB-2T (**b**) inversion for stomatal conductance (g_s) estimations against in-situ observations measured with handheld porometer (LI-600) across all sampling dates in 2023

for each pairwise comparison, including demonstrating a non-significant difference between 0.2 and 0.4 Kc treatments (*p value* = 0.12).

Estimation of gst through TSEB inversion

Leaf stomatal conductance (g_{st}) was estimated by inverting both TSEB-PT and TSEB-2T fluxes and were compared against in-situ leaf-level measurements (Fig. 6). Considering the scaling difficulty of comparing downscaled ecosystem-level fluxes (TSEB outputs) and upscaled leaf-level measurements (in-situ), modelled results agreed reasonably well, where values were within similar ranges to in-situ measurements with low bias (TSEB-PT bias = 0.1 mol m^{-2} s^{-1}; TSEB-2T bias = 0.05 mol m^{-2} s^{-1}). TSEB-2T achieved higher correlation (r = 0.35) than TSEB-PT but larger dispersion and errors (RMSE = 0.11 mol m^{-2} s^{-1}; rRMSE = 46%). However, the largest biases for TSEB-2T were primarily concentrated during early and late phenological periods. By solely evaluating the results of the UAV flights during the peak growth period (2023-07-18, 2023-08-01 and 2023-08-16), as shown in Fig. 7, TSEB-2T errors decreased (RMSE = 0.05 mol m^{-2} s^{-1}; rRMSE = 20%) and showed higher correlation (r = 0.59). By contrast, TSEB-PT, although with low errors and biases, did not capture as much variability during this peak growth period (r = 0.28). This result is likely due to TSEB-PT LEc/LE values having little change with treatment.

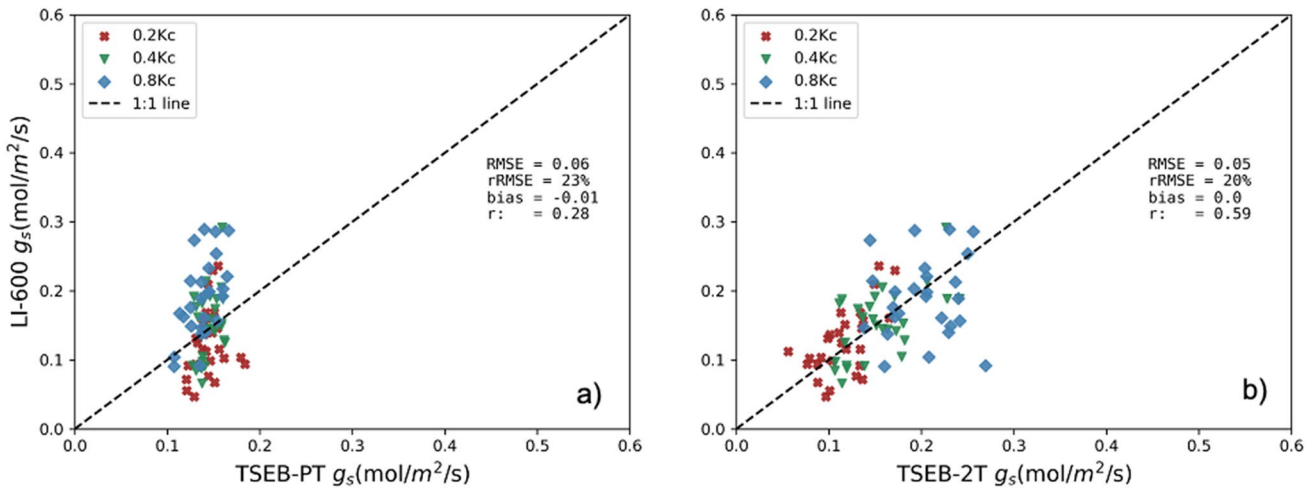

Fig. 7 Evaluation of TSEB-PT (**a**) and TSEB-2T (**b**) inversion for stomatal conductance (g_s) estimations against in-situ observations measured with handheld porometer (LI-600) during the peak vegetation growth period (2023-07-18, 2023-08-01 and 2023-08-16)

Performance of different stress indices compared to in-situ measurements

Figures 8 and 9 illustrate the relationship between bulk crop water stress indices computed with TSEB-PT and TSEB-2T, respectively and in-situ Ψ_{leaf} and Ψ_{stem} measurements. Results follow very similar patterns with little difference between stress indices and between TSEB-2T and TSEB-PT. CWSI-PM was most related to Ψ_{stem} with both TSEB-PT ($\rho = 0.56$) and TSEB-2T ($\rho = 0.57$). In general, we observed that stress indices based on bulk fluxes tend to plateau for lowest Ψ_{stem} values ($\Psi_{stem} < -1.0$ Mpa), indicating that perhaps the UAV-based stress indicators were less able to capture the variability of highly stressed plants. Ψ_{leaf} was generally less related to stress indices ($\rho < 0.4$) with the highest score achieved by TSEB-2T with CWSI-SW ($\rho = 0.4$).

By contrast, when comparing the crop water stress indices computed with partitioned or canopy fluxes (i.e. LEc, CTSI, CSSI), large differences were observed between TSEB-PT and TSEB-2T (Fig. 10 vs Fig. 11). In general, TSEB-PT based stress indices based on canopy fluxes had low correlation with Ψ_{leaf} and Ψ_{stem}, with the highest correlation observed between with CTSI and Ψ_{stem} ($\rho = 0.49$). TSEB-2T stress indices generally achieved higher correlation with Ψ_{leaf} ($\rho > 0.4$) and Ψ_{stem} ($\rho > 0.6$), where the highest correlation was observed between CSSI and Ψ_{stem} ($\rho = 0.62$).

Discussion

The results from this study indicated that TSEB, either through TSEB-PT or TSEB-2T, was capable of reliably estimating energy fluxes through UAV imagery with RMSE

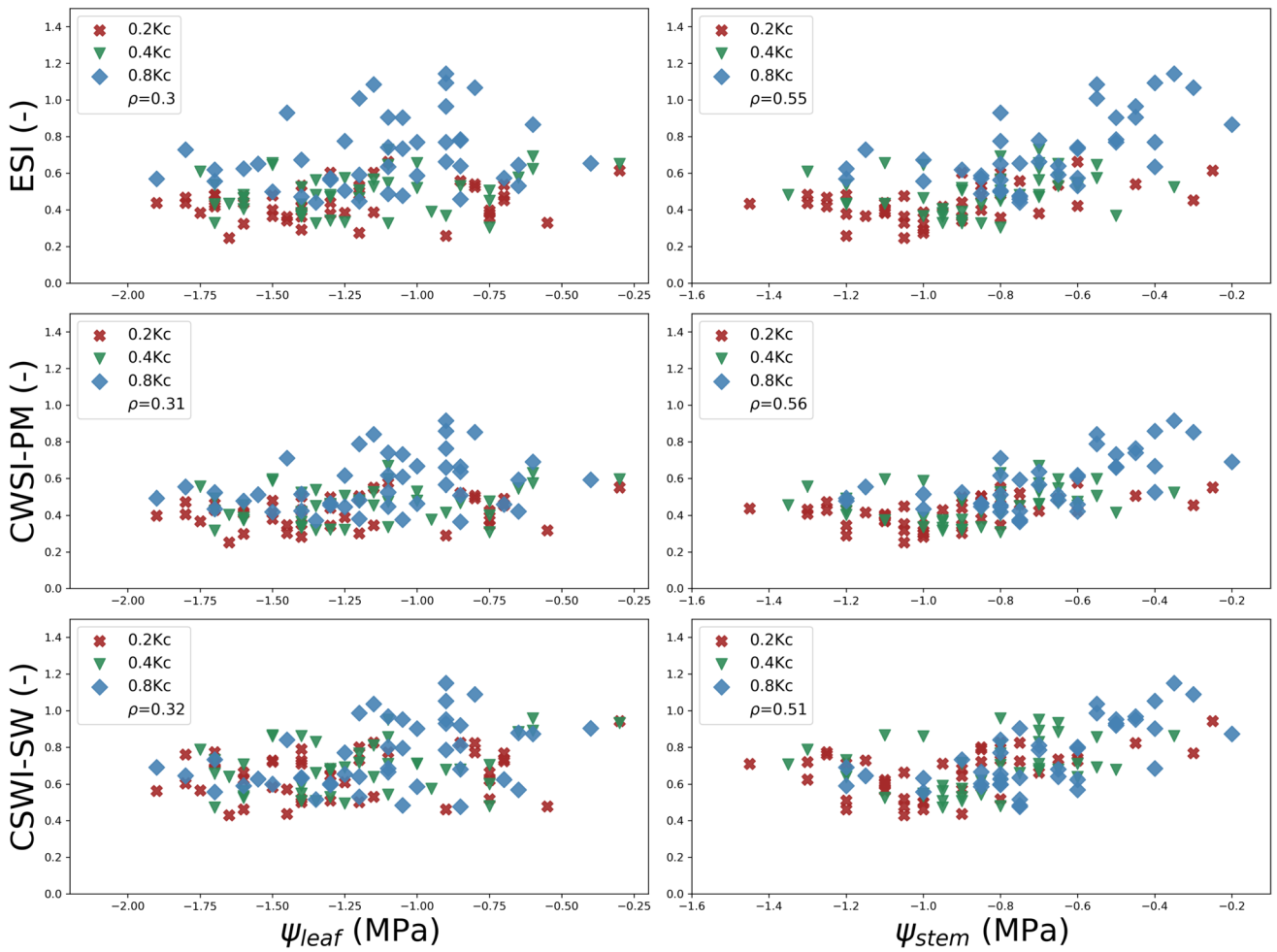

Fig. 8 TSEB-PT crop water stress indexes (CWSI) using bulk fluxes against in-situ measurements of leaf (Ψ_{leaf}) and stem (Ψ_{stem}) water potential

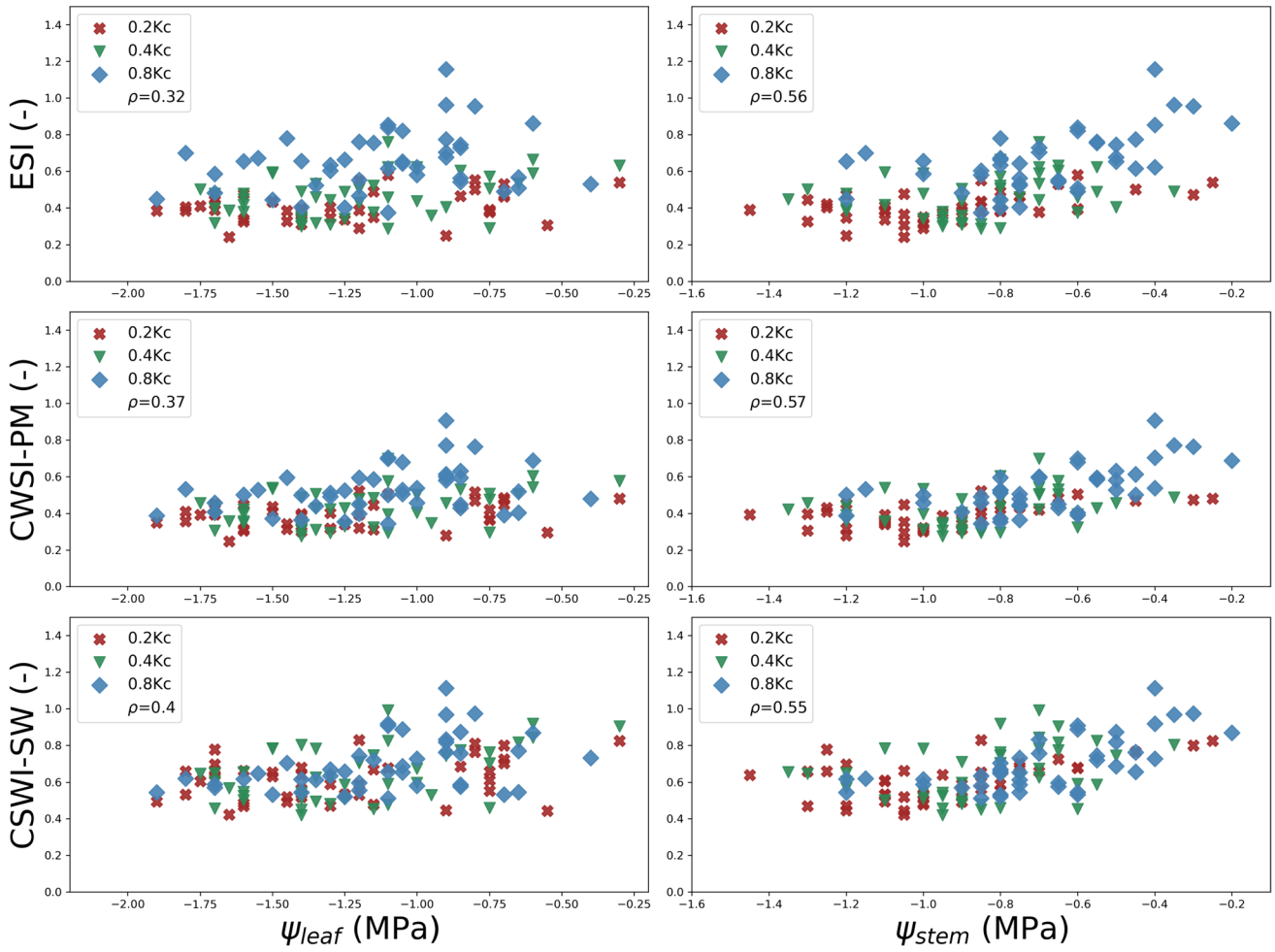

Fig. 9 TSEB-2T crop water stress indexes (CWSI) using bulk fluxes against in-situ measurements of leaf (Ψ_{leaf}) and stem (Ψ_{stem}) water potential

bounds within 25–80 W/m^2 compared to EC measurements. These errors are within the expected uncertainties for the models and measurements (50–100 W/m^2) and are within similar ranges compared to other studies in vineyards (Gao et al. 2023; Kustas, et al. 2022; Nieto et al. 2019, 2022). For instance, LE errors using UAVs and different TSEB model versions were reported by Gao et al. (2023) to be between 69–90 W/m^2 for vineyards in California while Ortega-Farias et al. (2021) obtained an RMSE of 55 W/m^2 using a two-source patch energy balance model in a Chilean vineyard site. Similar error ranges (i.e., roughly 60 W/m^2) were also reported by Simpson et al. (2022) for a savanna ecosystem in Spain applying TSEB with over 25 UAV overpasses and evaluated using 6 different EC towers. Therefore, the results and energy flux uncertainties presented in this study were very much in agreement with similar studies available in the literature. However, the in-situ EC measurements are also expected to have their own uncertainties, especially since the tower footprint overlaps at least two different irrigation treatments leading to a certain level of heterogeneity, which may not be captured as effectively by the net radiometer or the soil heat flux plates. For example, while the five soil heat flux plates were installed cross sectionally between two treatments, this sampling design may not effectively capture the G heterogeneity present in the flux footprint, which must account for both irrigation treatment effects but also differences between the row crop and interrow since the drip irrigation applies the water input locally near grapevine. As such, there is likely additional uncertainties related to the estimation of the available energy compared to sampling over a uniform site, even though the estimated Rn and G compared rather well to tower measurements (Fig. 2, Table 2). Furthermore, the widely acknowledged energy balance closure issue (Bambach et al. 2022; Mauder et al. 2020) is another source of uncertainty and it is worth noting that the largest discrepancy between modelled and measured H occurred on the date with lowest energy balance closure (i.e. 0.58).

The different stress indicators estimated through bulk fluxes (i.e. CWSI-PM, CWSI-SW and ESI) related similarly

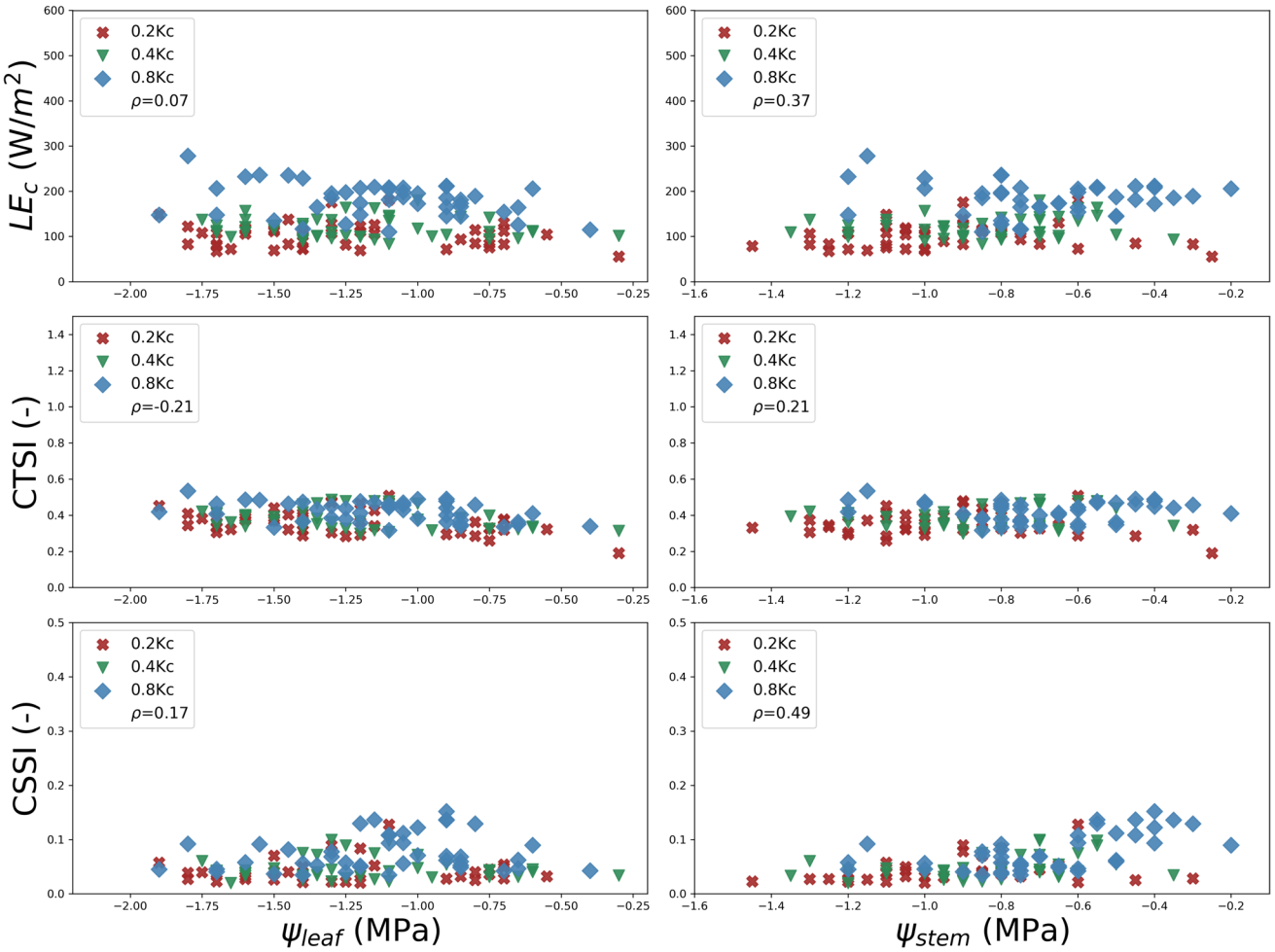

Fig. 10 TSEB-PT crop water stress indexes (CWSI) using partitioned canopy latent heat fluxes (LEc) against in-situ measurements of leaf (Ψ_{leaf}) and stem (Ψ_{stem}) water potential

to in-situ measurements, either applied with TSEB-PT or TSEB-2T. The CWSI-PM yielded slightly better results compared to CWSI-SW, showing little evidence of the advantage of using the SW model to compute potential LE (LE_{pot}) compared to PM, even though its dual-source model structure should be more suited for clumped row vegetation structures such as grapevines. As Nieto et al. (2022) noted, this may be an issue of how LE_{pot} is defined, where, in this study, we parameterized LE_{pot} in the SW model as having a rather constant dry top soil but with enough water in the root-zone for vegetation to transpire at a potential rate. It is likely that the assumption of a very dry soil was not adequate for all the different UAV campaigns assessed here, with soil conditions being affected by seasonal changes and, in certain cases, by precipitation events occurring relatively close in time to the field campaigns, especially during the first campaign of 2023. Soil conditions not only affects the bulk LE (through soil evaporation) but also interacts with the canopy fluxes as it influences the evaporative demand in the canopy by transporting hot (or cool) and dry (or wet) air parcels from the soil towards the canopy-air interface (Kustas and Norman 1999).

The crop water stress indicators that took advantage of modelled canopy fluxes (CTSI and CSSI) showed large differences between TSEB-PT and TSEB-2T. The CTSI and CSSI estimated by TSEB-PT were much less correlated with in-situ measurements, with the highest correlation achieved by CSSI and Ψ_{stem} ($\rho = 0.49$). On the other hand, the CTSI and CSSI estimated by TSEB-2T were much more correlated with in-situ measurements, with both yielding better results compared to the indices based on bulk fluxes (i.e., CWSI-PM, CWSI-SW or ESI). In fact, CSSI had the highest correlation out of all studied indices with both Ψ_{leaf} ($\rho = 0.43$) and Ψ_{stem} ($\rho = 0.61$). These correlations are largely in line with results presented in Bellvert et al. (2020) which reported an R^2 ranging from 0.29 to 0.55 between a transpiration-based CWSI and Ψ_{stem}. Indeed, Bellvert et al. (2020) also showed that the relationship between Ψ_{stem} and canopy transpiration

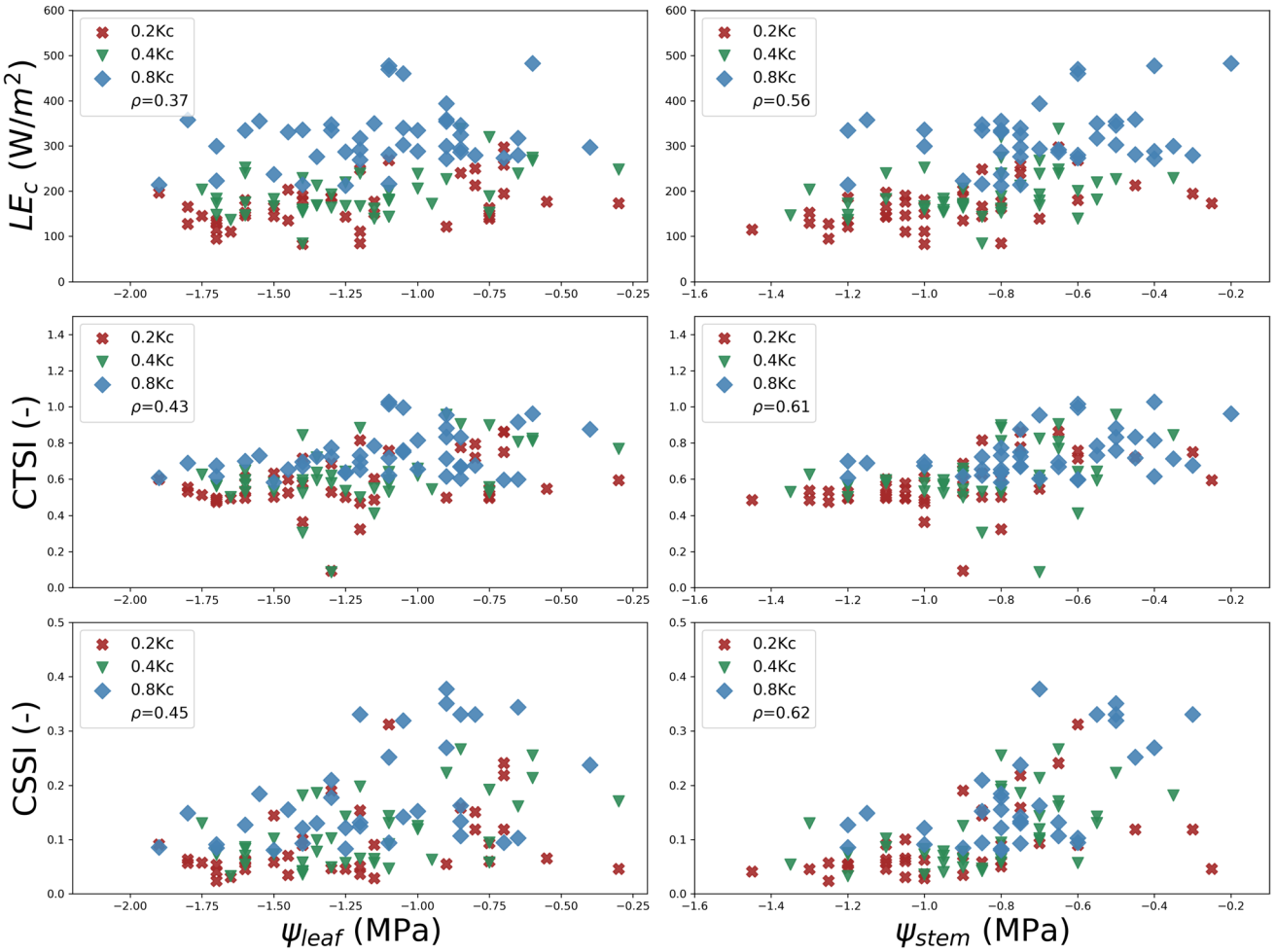

Fig. 11 TSEB-2T crop water stress indexes (CWSI) using partitioned canopy latent heat fluxes (LEc) against in-situ measurements of leaf (Ψ_{leaf}) and stem (Ψ_{stem}) water potential

was stronger and more consistent compared to bulk ET in vineyards, as estimated through TSEB with both satellite and airborne imagery. These results, along with the results presented in Nieto et al. (2022) demonstrate the potential of using partitioned canopy fluxes to limit the effect of the soil signal on CWSI and to improve crop water stress detection using remote sensing.

In general, Ψ_{stem} was more correlated ($\rho > 0.5$) to UAV ET-based stress indices compared to Ψ_{leaf} ($\rho < 0.4$). The poor results with Ψ_{leaf} were also observed by Nieto et al. (2022), while several studies have highlighted the limitation of Ψ_{leaf} to robustly represent water stress (García-Tejera et al. 2021; Jones 2004). Clearly, one of the main limitations is that these measurements are highly sensitive to plant architecture with different management interventions, such as vine pruning, affecting the hydraulic conductivity from the root to leaf. As such, Ψ_{leaf} at different phenological periods may be more affected by structural changes than to water stress. For example, Bellvert et al. (2015) showed that the relationship between CWSI and Ψ_{leaf} was significantly affected by both the grapevine variety and phenological stage, requiring model calibration to account for these effects.

Several authors have suggested the use of g_{st} rather than water potential for water stress detection as it accounts for crop physiology within atmospheric conditions, along with linking the processes of transpiration and photosynthesis (Jarvis 1986). Nieto et al. (2022) demonstrated TSEB's effectiveness to estimate g_{st} through flux inversion and tower-based inputs, which compared well with in-situ measurements of leaf gas exchange. In this study, we also show that TSEB-based g_{st} estimated through UAV imagery were within similar error ranges (RMSD ~ 0.1 mol m^{-2} s^{-1}) compared to in-situ leaf measurements, although we observed a lower correlation ($r < 0.35$). There was also a large difference between TSEB-PT and TSEB-2T, where g_{st} estimated by TSEB-PT showed much less variability, likely affected from the apparent underestimation of LEc (Fig. 3). This was particularly apparent when solely evaluating the peak

vine growth period (Fig. 5) where TSEB-2T very effectively estimated g_{st} during this period (RMSE = 0.05 mol m^{-2} s^{-1}; r = 0.59) compared to TSEB-PT (RMSE = 0.06 mol m^{-2} s^{-1}; r = 0.28). The larger errors during the early and late phenological periods may be related to (i) lower f_g·LAI values during these dates, that might cause arithmetic instability when inverting Eq. 7 and (ii) the greater difficulty to measure in-situ g_{st} since fewer well-developed leaves are present or, especially for late phenological period, may be diseased or damaged. In fact, there is an implicit bias to sample well illuminated and healthy leaves, which also depends on the subjectivity of the operator, while the UAV imagery samples the entire top of the canopy, composed of leaves with varying conditions including being sunlit and shaded. Jones et al. (2002) demonstrated significant differences in g_{st} between sunlit and shaded leaves, with sunlit leaves having, on average, double the g_{st} values as shaded leaves. As such, there is an inherent difficulty in comparing top-down ecosystem-level fluxes (TSEB outputs) and leaf-level measurements (in-situ), which can be a factor that increases the scatter of results observed between the UAV imagery and the leaf-scale measurements.

Large differences in modelled LE partitioning (LEc/LE) between TSEB-PT and TSEB-2 T were apparent in this study, both by evaluating CTSI and CSSI against in-situ indicators (Fig. 9 vs Fig. 10) and by observing the spatial variability and sensitivity to treatment effects (Fig. 4). TSEB-PT showed on average a much lower LEc/LE (~0.4) compared to TSEB-2T (~0.8). Burchard-Levine et al. (2022) reported a LEc/LE of about 0.8 during the main grapevine growing season in California, USA, both by applying an adapted TSEB version (three-source energy balance model, 3SEB) and an EC-based partitioning method (Zahn et al. 2022). Kustas et al. (2019) also reported a monthly LEc/LE between 0.8 and 0.9 during the summer months as estimated from EC partitioning method (Scanlon and Kustas 2012) and showed that TSEB-PT, forced from tower-based inputs, largely underestimated LEc/LE with values below 0.6 during these periods. Using UAV imagery, Gao et al. (2023) also compared TSEB-PT and TSEB-2T in a vineyard and showed that LEc/LE was better depicted by TSEB-2T, especially when applying the so-called quantile temperature separation algorithm to better extract Tc from the canopy. By contrast, using tower-based measurements, Kool et al. (2021) showed that TSEB-PT was more reliable than TSEB-2T for LEc/LE retrievals. At the satellite level, when comparing the atmosphere–land exchange inverse model (ALEXI) model, based on TSEB, using both a PT and PM initialization, Knipper et al., (2022) also revealed that the PT initialization had greater uncertainty for LEc/LE compared to the PM initialization, even though bulk fluxes were well simulated. Indeed, our results, along with past studies, show that TSEB's ET partitioning is sensitive to the initial transpiration parameterization, necessary to decompose LST into canopy and soil sources when the pixel is mixed by both components. Future work should concentrate on better understanding the effect of the different transpiration initialization, such as using a PM (Colaizzi et al. 2014) or SW (Kustas, et al. 2022) parameterization, and understand the respective sensitivity of input variables affecting LEc/LE estimations.

Conclusion

These results demonstrate the utility of physically-based models (i.e. TSEB) and UAV imagery to estimate ET and partitioned canopy fluxes, which can enhance the detection of vine water stress. Moreover, the results indicate satisfactory congruence of modelled energy fluxes compared to a reference EC tower. Modelled bulk fluxes were able to depict irrigation treatment effects and were somewhat correlated to in-situ measurements (more notably with Ψ_{stem}). However, partitioned flux indicators, by better isolating the vegetation signal and limiting soil/substrate effects, were more effective in detecting these irrigation treatment effects and had higher correlation to in-situ water stress proxies, including comparing well to in-situ g_{st} measurements. Since TSEB-2T and TSEB-PT showed large differences in modelled LEc/LE, future work should concentrate on better evaluating the modelled ET partitioning. This includes testing different TSEB transpiration formulations and soil and canopy temperature partitioning methods, to better understand the effects of the different model initializations on LEc/LE estimates, especially under different agronomic (e.g. presence of cover crop) and climatic conditions. This includes better understanding the effect of advection present in many irrigated agricultural regions as explored by Kustas et al. (2022).

Appendix A

See Figs. 12 and 13

Appendix B

The Penman–Monteith (PM) model combines aerodynamic theory with surface energy balance using a 'big leaf' framework assuming a single plane within the vegetation as a source and sink for mass and energy transfer. The general PM equation is expressed as:

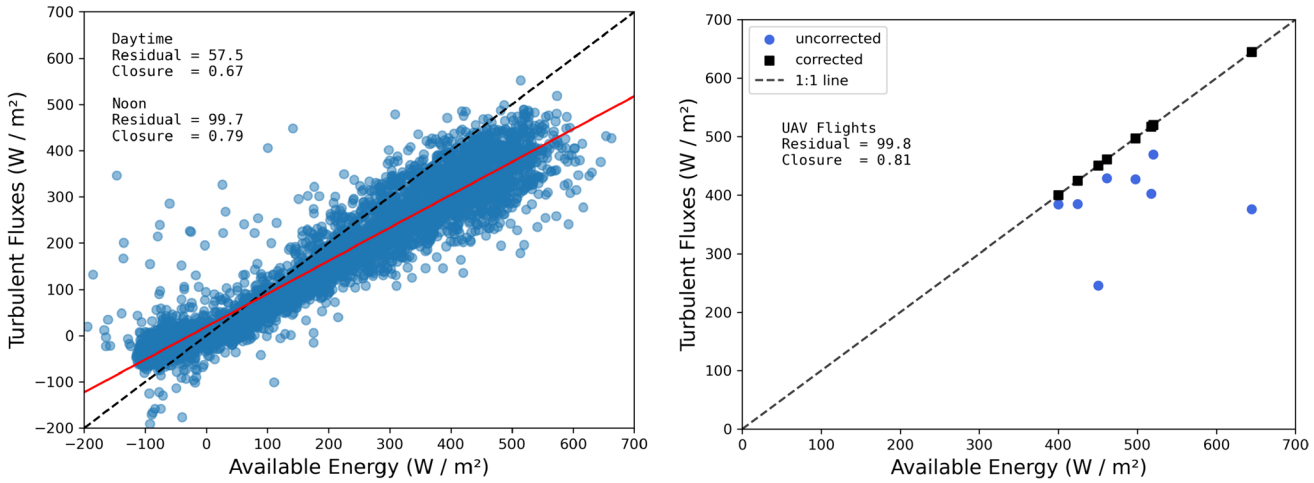

Fig. 12 Energy balance closure of the half-hourly available energy (Rn-G) and turbulent fluxes (H+LE) over the entire sampling period (2022-08-04 to 2022-09-19) (left panel) and during the time steps corresponding to the UAV overpasses (right panel)

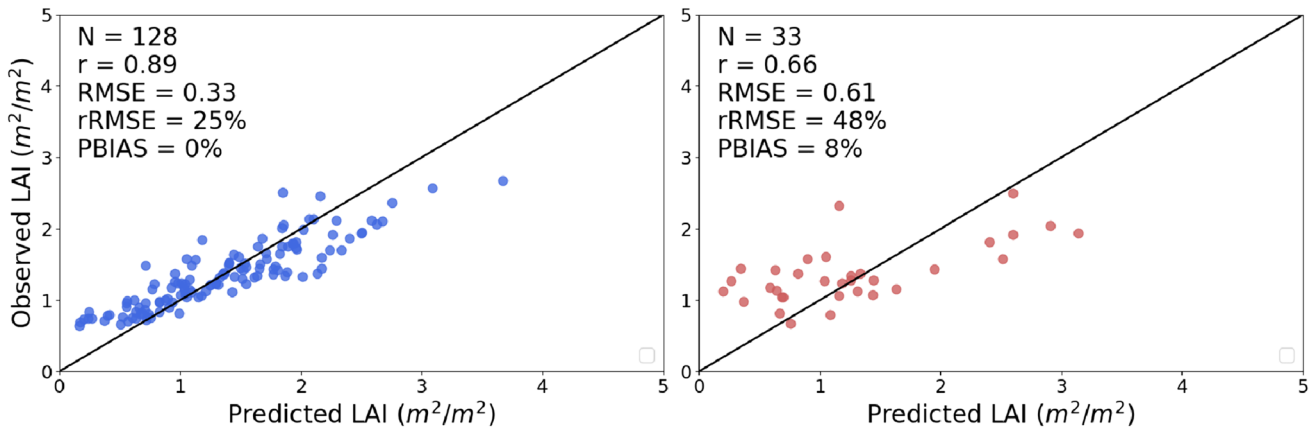

Fig. 13 Calibration (left panel) and validation (right panel) of random forest LAI model applied with OSAVI, reNDVI, canopy height (CH) and fractional cover (fc) inputs and trained with in-situ LAI measurements using the LAI-2200C (*LI-COR Biosciences, Lincoln, NE*). Dataset was divided 80/20 between calibration and validation groups

$$LE = \frac{\Delta(Rn - G) + \rho C_p\left(\frac{VPD}{R_{AH}}\right)}{\Delta + \gamma\left(\frac{R_c}{R_{AH}}\right)} \quad \text{(B1)}$$

Where $\Delta = \Delta e_s/\Delta T_A$ and is the slope of the saturation vapor pressure curve with respect to air temperature, VPD is the atmospheric vapor presure deficit. To obtain a potential LE, a fixed R_c may be used (i.e. 50 s m^{-1}) as described in Colaizzi et al. (2012, 2014). However, in this study, we implemented an estimation of R_c that depends on VPD, where vegetation more coupled to the atmosphere, such as taller tree crops, have shown more sensitivity to VPD conditions. As such, R_c was estimated based on parametrization proposed by Montheith (1995) as described in Kustas et al. (2022).

To account for conditions of sparse vegetation where both soil and vegetation contribute significantly to LE, the Shuttleworth-Wallace (SW) model was developed as two-source energy combination model, which is based on PM-like equations. The canopy latent heat flux (or transpiration) is computed as:

$$LEc = \frac{\Delta Rn, c + \rho C_p\left(\frac{VPD_0}{R_x}\right)}{\Delta + \gamma\left(\frac{R_c}{R_x}\right)} \quad \text{(B2)}$$

where VPD_0 is the vapor pressure deficit at the canopy-air interface and is estimated as:

$$VPD_0 = VPD + R_{AH}\frac{\Delta(Rn-G)-(\Delta+\gamma)LE}{\rho c_p} \quad \text{(B3)}$$

LE is estimated through the general form of SW:

$$LE = C_c PM_C + C_S PM_S \quad \text{(B4)}$$

$$PM_c = \frac{\Delta(Rn-G)+\left[\frac{\rho C_p VPD-\Delta R_x(Rn,s-G)}{R_{AH}+R_x}\right]}{\Delta+\gamma\left(1+\frac{R_c}{R_{AH}+R_x}\right)} \quad \text{(B5)}$$

$$PM_s = \frac{\Delta(AE)+\left[\frac{\rho C_p VPD-\Delta R_s Rn,c}{R_{AH}+R_s}\right]}{\Delta+\gamma\left(1+\frac{R_{ss}}{R_{AH}+R_s}\right)} \quad \text{(B6)}$$

The PMc and PMs are PM-like equations that describe the LE expressions from the canopy and soil sources, respectively; Cc and Cs are weighing factors based on the canopy and soil effective resistance terms, respectively (see Shuttleworth & Wallace (1985) for their derivations), The model describes five resistances to vapour flow: canopy stomatal resistance to water transport (R_c), bulk aerodynamic resistance to heat and water transport to the canopy elements (R_x), aerodynamic resistance to heat and water transport between the source-sink height and reference level (R_{AH}) and soil aerodynamic resistance to heat and water transport (R_s), soil surface resistance to water transport (R_{ss}). When computing potential LE, the latter is fixed to $R_{ss} = 2000 s\ m^{-1}$ to consider a rather dry soil surface, consistent with the definition of potential LE used with the PM approach.

Acknowledgements This research was supported by the DATI project (PCI2021-121932) from the Spanish Ministry of Science and Innovation (AEI/https://doi.org/10.13039/501100011033) and the PRIMA EU program. This work was also supported by the EO4WUE research project (TED2021-129814B-I00) funded by MCIN/AEI/https://doi.org/10.13039/501100011033 and by the European Union NextGenerationEU/PRTR. The authors VBL and IBS were financed by the grant FJC2021-047273-I and FJC2021-047687-1, respectively, funded by MCIN/AEI/https://doi.org/10.13039/501100011033 and European Union NextGenerationEU/PRTR, while the authors GMR has been a beneficiary of a FPI fellowship by the Spanish Ministry of Education and Professional Training (PRE2018-083227). The authors thank the technicians David Campos and José Manuel Martín, members of the Tech4agro research group, for their support during field sampling. We also thank IMIDRA's technical staff for maintaining experimental infrastructure at the *El Socorro* experimental farm. USDA is an equal opportunity provider and employer.

Author contributions VBL wrote the manuscript, analyzed the data and prepared all the figures in the manuscript. JMP and AIC acquired project funding, designed the experiment, acquired in-situ data and revised the manuscript. IBS processed UAV data, led field campaigns and revised the manuscript. HN conceptualized the analysis, provided support on energy balance modeling, data processing and in-situ sampling protocols/acquisitions. WPK supported with research infrastructure, support on energy balance modeling concepts/ideas and revised the manuscript. LMM supported with research infrastructure and EC data processing. JGG led field campaigns, processed in-situ data and revised the manuscript. JD supported experimental design, acquired in-situ data and revised the manuscript. GMR, MH and BM acquired and analyzed in-situ data and revised the manuscript. SSE helped design the experiment and supported with the research infrastructure.

Funding Open Access funding provided thanks to the CRUE-CSIC agreement with Springer Nature. Spanish Ministry of Science and Innovation and PRIMA EU, PCI2021-121932, PCI2021-121932, PCI2021-121932, PCI2021-121932, PCI2021-121932, PCI2021-121932, Spanish Ministry of Science and Innovation & European Union Next Generation EU/PRTR, FJC2021-047273-I ,FJC2021-047687-1 ,TED2021-129814B-I00, TED2021-129814B-I00, Spanish Ministry of Education and Professional Training, PRE2018-083227.

Data availability The dataset related to the results presented in this article are available here: http://hdl.handle.net/10261/354889. The modeling results were obtained using pyTSEB (https://github.com/hectornieto/pyTSEB).

Declarations

Conflict of interest The authors declare no competing interests.

References

Allen RG, Pereira LS, Raes D, Smith M et al (1998) Crop evapotranspiration-guidelines for computing crop water requirements-FAO Irrigation and drainage paper 56. FAO, Rome 300(9):D05109

Allen RG, Tasumi M, Trezza R (2007) Satellite-based energy balance for mapping evapotranspiration with internalized calibration (METRIC)—model. J Irrig Drain Eng 133:380–394

Bambach N, Kustas W, Alfieri J, Prueger J, Hipps L, McKee L, Castro SJ, Volk J, Alsina MM, McElrone AJ (2022) Evapotranspiration uncertainty at micrometeorological scales: the impact of the eddy covariance energy imbalance and correction methods. Irrig Sci 40(4):445–461. https://doi.org/10.1007/s00271-022-00783-1

Bellvert J, Marsal J, Girona J, Zarco-Tejada PJ (2015) Seasonal evolution of crop water stress index in grapevine varieties determined with high-resolution remote sensing thermal imagery. Irrig Sci 33(2):81–93. https://doi.org/10.1007/s00271-014-0456-y

Bellvert J, Marsal J, Girona J, Gonzalez-Dugo V, Fereres E, Ustin S, Zarco-Tejada P (2016) Airborne thermal imagery to detect the seasonal evolution of crop water status in peach, nectarine and saturn peach orchards. Remote Sens 8(1):39. https://doi.org/10.3390/rs8010039

Bellvert J, Jofre-Ĉekalović C, Pelechá A, Mata M, Nieto H (2020) Feasibility of using the two-source energy balance model (TSEB)

with sentinel-2 and sentinel-3 images to analyze the spatio-temporal variability of vine water status in a vineyard. Remote Sens 12(14):2299. https://doi.org/10.3390/rs12142299

Burchard-Levine V, Nieto H, Kustas WP, Gao F, Alfieri JG, Prueger JH, Hipps LE, Bambach-Ortiz N, McElrone AJ, Castro SJ, Alsina MM, McKee LG, Zahn E, Bou-Zeid E, Dokoozlian N (2022) Application of a remote-sensing three-source energy balance model to improve evapotranspiration partitioning in vineyards. Irrig Sci. https://doi.org/10.1007/s00271-022-00787-x

Colaizzi PD, Evett SR, Howell TA, Tolk JA (2004) Comparison of aerodynamic and radiometric surface temperature using precision weighing lysimeters. In: Gao W, Shaw DR (eds) Remote sensing and modeling of ecosystems for sustainability. SPIE, Bellingham, WA, p 215. https://doi.org/10.1117/12.559503

Colaizzi PD, Evett SR, Howell TA, Li F, Kustas WP, Anderson MC (2012) Radiation model for row crops: I. geometric view factors and parameter optimization. Agron J 104(2):225–240

Colaizzi PD, Agam N, Tolk JA, Evett SR, Howell TA, Gowda PH, O'Shaughnessy SA, Kustas WP, Anderson MC (2014) Two-source energy balance model to calculate E, T, and ET: comparison of priestley-taylor and penman-monteith formulations and two time scaling methods. Trans ASABE 57:479–498

Coombe BG, McCarthy MG (2000) Dynamics of grape berry growth and physiology of ripening. Aust J Grape Wine Res 6(2):131–135. https://doi.org/10.1111/j.1755-0238.2000.tb00171.x

de Castro AI, Shi Y, Maja JM, Peña JM (2021) UAVs for vegetation monitoring: overview and recent scientific contributions. Remote Sens 13(11):2139

Escalona JM, Flexas J, Medrano H (2000) Stomatal and non-stomatal limitations of photosynthesis under water stress in field-grown grapevines. Funct Plant Biol 27(1):87–87. https://doi.org/10.1071/pp99019_co

Farquhar GD, Sharkey TD (1982) Stomatal conductance and photosynthesis. Annu Rev Plant Physiol 33(1):317–345. https://doi.org/10.1146/annurev.pp.33.060182.001533

Gao R, Torres-Rua AF, Nieto H, Zahn E, Hipps L, Kustas WP, Alsina MM, Bambach N, Castro SJ, Prueger JH, Alfieri J, McKee LG, White WA, Gao F, McElrone AJ, Anderson M, Knipper K, Coopmans C, Gowing I, Dokoozlian N (2023) ET partitioning assessment using the TSEB model and sUAS information across california central valley vineyards. Remote Sens 15(3):756 (**Article 3**)

García-Tejera O, López-Bernal Á, Orgaz F, Testi L, Villalobos FJ (2021) The pitfalls of water potential for irrigation scheduling. Agric Water Manag 243:106522. https://doi.org/10.1016/j.agwat.2020.106522

Girona J, Mata M, del Campo J, Arbonés A, Bartra E, Marsal J (2006) The use of midday leaf water potential for scheduling deficit irrigation in vineyards. Irrig Sci 24(2):115–127. https://doi.org/10.1007/s00271-005-0015-7

Gitelson A, Merzlyak MN (1994) Spectral reflectance changes associated with autumn senescence of aesculus hippocastanum L. and acer platanoides L. leaves. spectral features and relation to chlorophyll estimation. J Plant Physiol 143(3):286–292

Gonzalez-Dugo V, Zarco-Tejada PJ (2022) Assessing the impact of measurement errors in the calculation of CWSI for characterizing the water status of several crop species. Irrig Sci. https://doi.org/10.1007/s00271-022-00819-6

Guerra JG, Cabello F, Fernández-Quintanilla C, Peña JM, Dorado J (2022) Use of under-vine living mulches to control noxious weeds in irrigated mediterranean vineyards. Plants 11(15):1921

Jackson RD, Idso SB, Reginato RJ, Pinter PJ (1981) Canopy temperature as a crop water stress indicator. Water Resour Res 17(4):1133–1138. https://doi.org/10.1029/WR017i004p01133

Jarvis PJ (1986) Coupling of carbon and water interactions in forest stands. Tree Physiol 2(1–2–3):347–368. https://doi.org/10.1093/treephys/2.1-2-3.347

Jones HG (2004) Irrigation scheduling: advantages and pitfalls of plant-based methods. J Exp Bot 55(407):2427–2436. https://doi.org/10.1093/jxb/erh213

Jones HG, Stoll M, Santos T, de Sousa C, Chaves MM, Grant OM (2002) Use of infrared thermography for monitoring stomatal closure in the field: application to grapevine. J Exp Bot 53(378):2249–2260

Kang Y, Gao F, Anderson M, Kustas W, Nieto H, Knipper K, Yang Y, White W, Alfieri J, Torres-Rua A, Alsina MM, Karnieli A (2022) Evaluation of satellite leaf area index in California vineyards for improving water use estimation. Irrig Sci 40(4–5):531–551. https://doi.org/10.1007/s00271-022-00798-8

Kljun N, Calanca P, Rotach MW, Schmid HP (2015) A simple two-dimensional parameterisation for flux footprint prediction (FFP). Geoscientific Model Development 8(11):3695–3713. https://doi.org/10.5194/gmd-8-3695-2015

Knipper KR, Kustas WP, Anderson MC, Alsina MM, Hain CR, Alfieri JG, Prueger JH, Gao F, McKee LG, Sanchez LA (2019) Using high-spatiotemporal thermal satellite ET retrievals for operational water use and stress monitoring in a california vineyard. Remote Sens 11(18):2124. https://doi.org/10.3390/rs11182124. (**Article 18**)

Kool D, Kustas WP, Ben-Gal A, Agam N (2021) Energy partitioning between plant canopy and soil, performance of the two-source energy balance model in a vineyard. Agric for Meteorol 300:108328. https://doi.org/10.1016/j.agrformet.2021.108328

Kustas WP, Norman JM (1997) A two-source approach for estimating turbulent fluxes using multiple angle thermal infrared observations. Water Resour Res 33(6):1495–1508. https://doi.org/10.1029/97WR00704

Kustas WP, Norman JM (1999) Evaluation of soil and vegetation heat flux predictions using a simple two-source model with radiometric temperatures for partial canopy cover. Agric for Meteorol 94:13–29

Kustas WP, Nieto H, Morillas L, Anderson MC, Alfieri JG, Hipps LE, Villagarcía L, Domingo F, Garcia M (2016) Revisiting the paper "using radiometric surface temperature for surface energy flux estimation in mediterranean drylands from a two-source perspective." Remote Sens Environ 184:645–653. https://doi.org/10.1016/j.rse.2016.07.024

Kustas WP, Agam N, Ortega-Farias S (2019a) Forward to the GRAPEX special issue. Irrig Sci 37(3):221–226. https://doi.org/10.1007/s00271-019-00633-7

Kustas WP, Alfieri JG, Nieto H, Wilson TG, Gao F, Anderson MC (2019b) Utility of the two-source energy balance (TSEB) model in vine and interrow flux partitioning over the growing season. Irrig Sci 37(3):375–388. https://doi.org/10.1007/s00271-018-0586-8

Kustas WP, McElrone AJ, Agam N, Knipper K (2022a) From vine to vineyard: the GRAPEX multi-scale remote sensing experiment for improving vineyard irrigation management. Irrig Sci 40(4):435–444. https://doi.org/10.1007/s00271-022-00816-9

Kustas WP, Nieto H, Garcia-Tejera O, Bambach N, McElrone AJ, Gao F, Alfieri JG, Hipps LE, Prueger JH, Torres-Rua A, Anderson MC, Knipper K, Alsina MM, McKee LG, Zahn E, Bou-Zeid E, Dokoozlian N (2022b) Impact of advection on two-source energy balance (TSEB) canopy transpiration parameterization for vineyards in the california central valley. Irrig Sci. https://doi.org/10.1007/s00271-022-00778-y

Kustas WP, Anderson MC, Alfieri JG, Knipper K, Torres-Rua A, Parry CK, Nieto H, Agam N, White WA, Gao F, McKee L, Prueger JH, Hipps LE, Los S, Alsina MM, Sanchez L, Sams B, Dokoozlian N, McKee M, Hain C (2018) The grape remote sensing atmospheric

profile and evapotranspiration experiment. Bull Am Meteor Soc 99(9):1791–1812. https://doi.org/10.1175/BAMS-D-16-0244.1

Limier B, Ivorra S, Bouby L, Figueiral I, Chabal L, Cabanis M, Ater M, Lacombe T, Ros J, Bremond L (2018) Documenting the history of the grapevine and viticulture: a quantitative eco-anatomical perspective applied to modern and archaeological charcoal. J Archaeol Sci 100:45–61

Lorenz Dh, Eichhorn Kw, Bleiholder H, Klose R, Meier U, Weber E (1995) Growth stages of the grapevine: phenological growth stages of the grapevine (vitis vinifera L. ssp. vinifera)—codes and descriptions according to the extended BBCH scale. Aust J Grape Wine Res 1(2):100–103. https://doi.org/10.1111/j.1755-0238.1995.tb00085.x

Maes WH, Steppe K (2012) Estimating evapotranspiration and drought stress with ground-based thermal remote sensing in agriculture: a review. J Exp Bot 63(13):4671–4712. https://doi.org/10.1093/jxb/ers165

Mauder M, Foken T, Cuxart J (2020) Surface-energy-balance closure over land: a review. Bound-Layer Meteorol 177(2–3):395–426. https://doi.org/10.1007/s10546-020-00529-6

Nassar A, Torres-Rua A, Kustas W, Nieto H, McKee M, Hipps L, Stevens D, Alfieri J, Prueger J, Alsina MM, McKee L, Coopmans C, Sanchez L, Dokoozlian N (2020) Influence of model grid size on the estimation of surface fluxes using the two source energy balance model and sUAS imagery in vineyards. Remote Sens 12(3):342. https://doi.org/10.3390/rs12030342

Nieto H, Kustas WP, Torres-Rúa A, Alfieri JG, Gao F, Anderson MC, White WA, Song L, del Alsina MM, Prueger JH, McKee M, Elarab M, McKee LG (2019) Evaluation of TSEB turbulent fluxes using different methods for the retrieval of soil and canopy component temperatures from UAV thermal and multispectral imagery. Irrig Sci 37(3):389–406. https://doi.org/10.1007/s00271-018-0585-9

Nieto H, Alsina MM, Kustas WP, García-Tejera O, Chen F, Bambach N, Gao F, Alfieri JG, Hipps LE, Prueger JH, McKee LG, Zahn E, Bou-Zeid E, McElrone AJ, Castro SJ, Dokoozlian N (2022) Evaluating different metrics from the thermal-based two-source energy balance model for monitoring grapevine water stress. Irrig Sci 40(4):697–713. https://doi.org/10.1007/s00271-022-00790-2

Norman JM, Kustas WP, Humes KS (1995) Source approach for estimating soil and vegetation energy fluxes in observations of directional radiometric surface temperature. Agric for Meteorol 77:263–293

OIV. (2022). *State of the World Vine and Wine Sector 2021*. https://www.oiv.int/sites/default/files/documents/eng-state-of-the-world-vine-and-wine-sector-april-2022-v6_0.pdf. Accessed 2023–03–19

Ortega-Farias S, Esteban-Condori W, Riveros-Burgos C, Fuentes-Peñailillo F, Bardeen M (2021) Evaluation of a two-source patch model to estimate vineyard energy balance using high-resolution thermal images acquired by an unmanned aerial vehicle (UAV). Agric for Meteorol 304–305:108433. https://doi.org/10.1016/j.agrformet.2021.108433

Priestley CHB, Taylor RJ (1972) On the assessment of surface heat flux and evaporation using large-scale parameters. Mon Weather Rev 100(2):81–92. https://doi.org/10.1175/1520-0493(1972)100%3c0081:OTAOSH%3e2.3.CO;2

Raupach MR (1994) Simplified expressions for vegetation roughness length and zero-plane displacement as functions of canopy height and area index. Bound-Layer Meteorol 71:211–216

Rienth M, Scholasch T (2019) State-of-the-art of tools and methods to assess vine water status. Oeno One. https://doi.org/10.20870/oeno-one.2019.53.4.2403

Romero P, Navarro JM, Ordaz PB (2022) Towards a sustainable viticulture: the combination of deficit irrigation strategies and agroecological practices in mediterranean vineyards. a review and update. Agric Water Manag 259:107216

Rondeaux G, Steven M, Baret F (1996) Optimization of soil-adjusted vegetation indices. Remote Sens Environ 55(2):95–107

Scanlon TM, Kustas WP (2012) Partitioning evapotranspiration using an eddy covariance-based technique: improved assessment of soil moisture and land–atmosphere exchange dynamics. Vadose Zone Journal 11(3):vzj2012–vzj2025

Scholander PF, Hammel HT, Bradstreet ED, Hemmingsen EA (1965) Sap pressure in vascular plants. Science 148(3668):339–346

Shuttleworth WJ, Wallace JS (1985) Evaporation from sparse crops-an energy combination theory. QJR Meteorol Soc 111(469):839–855

Simpson JE, Holman FH, Nieto H, El-Madany TS, Migliavacca M, Martin MP, Burchard-Levine V, Cararra A, Blöcher S, Fiener P, Kaplan JO (2022) UAS-based high resolution mapping of evapotranspiration in a mediterranean tree-grass ecosystem. Agric for Meteorol 321:108981. https://doi.org/10.1016/j.agrformet.2022.108981

White WA, Alsina MM, Nieto H, McKee LG, Gao F, Kustas WP (2019) Determining a robust indirect measurement of leaf area index in california vineyards for validating remote sensing-based retrievals. Irrig Sci 37(3):269–280. https://doi.org/10.1007/s00271-018-0614-8

Xia T, Kustas WP, Anderson MC, Alfieri JG, Gao F, McKee L, Prueger JH, Geli HME, Neale CMU, Sanchez L, Alsina MM, Wang Z (2016) Mapping evapotranspiration with high-resolution aircraft imagery over vineyards using one- and two-source modeling schemes. Hydrol Earth Syst Sci 20(4):1523–1545. https://doi.org/10.5194/hess-20-1523-2016

Zahn E, Bou-Zeid E, Good SP, Katul GG, Thomas CK, Ghannam K, Smith JA, Chamecki M, Dias NL, Fuentes JD, Alfieri JG, Kwon H, Caylor KK, Gao Z, Soderberg K, Bambach NE, Hipps LE, Prueger JH, Kustas WP (2022) Direct partitioning of eddy-covariance water and carbon dioxide fluxes into ground and plant components. Agric for Meteorol 315:108790. https://doi.org/10.1016/j.agrformet.2021.108790